von Karman Institute for Fluid Dynamics

Lecture Series 1999-03

30^{TH} COMPUTATIONAL FLUID DYNAMICS

March 8 - 12, 1999

RANKINE-HUGONIOT-RIEMANN SOLVER AND CONVERGENCE ACCELERATION FOR LOW SPEED COMBUSTION

B. Müller[1] and P. Jenny[2]
[1]Uppsala University, Sweden
[2]Cornell University, Ithaca, New York, USA

Rankine-Hugoniot-Riemann Solver and Convergence Acceleration for Low Speed Combustion

B. Müller[a] and P. Jenny[b]
[a] *Department of Scientific Computing, Information Technology, Uppsala University, P.O. Box 120, S-751 04 Uppsala, Sweden*
[b] *Sibley School of Mechanical and Aerospace Engineering, Cornell University, Ithaca, New York 14853, USA*

Abstract

The Rankine-Hugoniot-Riemann (RHR) solver determines the inviscid fluxes for low speed combustion much more accurately than conventional Riemann solvers by taking into account source terms, viscous terms and multidimensional effects. The Mach number transformation accelerates the convergence of low Mach number reacting flow computations to steady-state by artificially lowering the speed of sound and thereby increasing the Mach number.

Key words: Navier-Stokes equations, source terms, combustion, low Mach number flow, thermoacoustics, finite volume method, approximate Riemann solver, multidimensional upwind scheme, convergence acceleration, steady-state, explicit scheme.

Notation: All physical quantities in this lecture are assumed to be dimensional and given in SI units.

Introduction

The interaction of heat release and sound is decisive for the operation of rocket motors, gas turbines, etc. According to Rayleigh's criterion, pressure is amplified, if heat release and pressure fluctuate in phase. This acoustic instability has to be controlled to avoid destruction of motors, turbines, etc. due to pressure amplification [1], [2], [3]. Since in many practical combustion applications the sound generation is primarily determined by entropy fluctuations in a slow turbulent flame, there has been considerable interest in low Mach number thermoacoustics [3].

The stability conditions of explicit compressible combustion codes are often dominated by the acoustic wave speeds, provided the stiff source terms are treated implicitly and the cell Reynolds number is high enough. For low Mach numbers, the inviscid stabilty condition is so limiting that many time steps are necessary for an entropy wave or a contact discontinuity to cross one cell. In subsonic laminar flames, the flame speed is generally much smaller than the speed of sound. Therefore, the number of time steps used by an explicit code to simulate flame propagation or to obtain steady-state is very large. Since steady-state solutions are interesting in themselves and are also often required as initial conditions of unsteady flow simulations, there is a great demand for such schemes. Thus, it is important to accelerate the convergence of low Mach number computations to the steady-state, in particular for low speed combustion.

The present lecture is based on Jenny's Ph.D. thesis [4] and articles by Jenny and Müller [5], [6], [7], [8].

The following section with the governing equations of reacting gas flow and their finite volume discretization constitutes the common basis of the two independent parts of this lecture.

In the first part, the Rankine-Hugoniot-Riemann (RHR) solver is explained to properly discretize the inviscid flux of the inhomogeneous Euler equations with the viscous terms and multidimensional effects contained in the stiff source term which describes chemical reactions.

In the second part, the Mach transformation is introduced to accelerate low speed combustion calculations to steady-state by artificially lowering the speed of sound and thereby increasing the Mach number.

The conclusions are stated in the third part.

Governing Equations

Thermodynamic, Transport and Chemical Models

We consider a thermally perfect gas mixture of n species M_i with the molecular weights W_i and the densities ρ_i. The mass fraction of species i (meaning M_i) is the ratio of the mass of species i and the mass of the mixture, i.e.

$$Y_i \;=\; \frac{\rho_i}{\rho}, \tag{1}$$

where ρ is the density of the mixture. Details of the thermodynamic model we used are given by Kuo [9].

Viscosity, molecular diffusion and heat conduction are described by simplified transport models. For the viscosity μ, we use the Sutherland law. The Schmidt numbers

$$Sc_i \;=\; \frac{\rho D_i}{\mu} \tag{2}$$

of all species are assumed to be equal and constant. D_i denotes the diffusion coefficient of species M_i and is determined from equation (2) by the specified Schmidt number and the computed density and viscosity. The Prandtl number

$$Pr \;=\; \frac{c_p \mu}{\kappa} \tag{3}$$

is assumed to be constant. c_p and κ are the specific heat at constant pressure and the heat conduction coefficient of the mixture, repectively.

We consider a chemical reaction mechanism with m reactions [9]. A reaction h (here h is an index for reactions and not the enthalpy) is of the form

$$\sum_{k=1}^{n} \nu'_{k,h} M_k \longrightarrow \sum_{k=1}^{n} \nu''_{k,h} M_k, \tag{4}$$

where $\nu'_{k,h}$ and $\nu''_{k,h}$ are the stoichiometric coefficients of reaction h for species k appearing as a reactant and as a product, respectively. The reaction rate of reaction h is

$$k_h \prod_{k=1}^{n} \left(\frac{\rho_k}{W_k}\right)^{\nu'_{k,h}} \tag{5}$$

with the Arrhenius term

$$k_h = \beta_h T^{\alpha_h} exp\left(\frac{-E_h^a}{R_u T}\right), \tag{6}$$

where α_h and β_h are constants and E_h^a is the activation energy of reaction h. R_u is the universal gas constant, and T is the temperature. The backward reaction of reaction (5) is

$$\left(\frac{k_h}{K_h^C}\right) \prod_{k=1}^{n} \left(\frac{\rho_k}{W_k}\right)^{\nu''_{k,h}}. \tag{7}$$

The equilibrium constants

$$K_h^C = \prod_{k=1}^{n} \left(\frac{\rho_k}{W_k}\right)_{equilibrium}^{(\nu''_{k,h} - \nu'_{k,h})} \tag{8}$$

are functions of temperature, and tables exist for most of them [10]. With the definitions above, the production rate ω_i of species i is given by

$$\omega_i = W_i \sum_{h=1}^{m} (\nu''_{i,h} - \nu'_{i,h}) k_h \left(\prod_{k=1}^{n} \left(\frac{\rho_k}{W_k}\right)^{\nu'_{k,h}} - \frac{1}{K_h^C} \prod_{k=1}^{n} \left(\frac{\rho_k}{W_k}\right)^{\nu''_{k,h}} \right). \tag{9}$$

2D Navier-Stokes Equations for Reacting Gas Flow

In Cartesian coordinates, the 2D compressible Navier-Stokes equations for reacting gas flow read in conservative form [9]

$$\frac{\partial \mathbf{U}}{\partial t} + \frac{\partial(\mathbf{F} - \mathbf{F}_v)}{\partial x} + \frac{\partial(\mathbf{G} - \mathbf{G}_v)}{\partial y} = \mathbf{S}, \tag{10}$$

where $\mathbf{U}$ is the vector of the conservative variables

$$\mathbf{U} = \begin{pmatrix} \rho_1 \\ \vdots \\ \rho_n \\ \rho u_1 \\ \rho u_2 \\ \rho E \end{pmatrix},$$

$\mathbf{F} = \mathbf{F}_1$ and $\mathbf{G} = \mathbf{F}_2$ are the inviscid flux vectors for the x- and y-directions with $\mathbf{F}_j$ defined by

$$\mathbf{F}_j = \begin{pmatrix} \rho_1 u_j \\ \vdots \\ \rho_n u_j \\ \rho u_1 u_j + p\delta_{1j} \\ \rho u_2 u_j + p\delta_{2j} \\ \rho H u_j \end{pmatrix},$$

$\mathbf{F}_v = \mathbf{F}_{v1}$ and $\mathbf{G_v} = \mathbf{F}_{v2}$ are the viscous flux vectors for the x- and y-directions with $\mathbf{F}_{vj}$ defined by

$$\mathbf{F}_{vj} = \begin{pmatrix} D_1 \rho \frac{\partial Y_1}{\partial x_j} \\ \vdots \\ D_n \rho \frac{\partial Y_n}{\partial x_j} \\ \tau_{1j} \\ \tau_{2j} \\ \sum_{l=1}^{2} u_l \tau_{lj} + \kappa \frac{\partial T}{\partial x_j} + \rho \sum_{k=1}^{n} \left(D_k h_k \frac{\partial Y_k}{\partial x_j} \right) \end{pmatrix}$$

and $\mathbf{S}$ is the source term

$$\mathbf{S} = \begin{pmatrix} \omega_1 \\ \vdots \\ \omega_n \\ 0 \\ 0 \\ \sum_{k=1}^{n} \left(\frac{\omega_k}{W_k} H_k^0 \right) \end{pmatrix}.$$

For a Newtonian fluid, the components of the shear stress tensor are
$\tau_{ij} = \mu \left(\frac{\partial u_i}{\partial x_j} + \frac{\partial u_j}{\partial x_i} \right) - \frac{2}{3}\mu \left(\sum_{k=1}^{2} \frac{\partial u_k}{\partial x_k} \right) \delta_{ij}$,
where $\delta_{ij} = 1$ if $i = j$ and $\delta_{ij} = 0$ if $i \neq j$. The Cartesian coordinates and velocity components are denoted by $(x_1, x_2)^T = (x, y)^T$ and $(u_1, u_2)^T = (u, v)^T$. p is the pressure, E the total energy per unit mass and H the total enthalpy. h_k is the averaged enthalpy of species k. H_k^0 is the standard heat of formation of species k.

Integrating equation (10) over a control volume Ω (actually a surface in 2D) with the boundary $\partial\Omega$ and the outer normal unit vector $\mathbf{n} = (n_x, n_y)^T$ and using the Gauss theorem, we obtain the integral form of the 2D Navier-Stokes equations for a reacting gas flow

$$\int_\Omega \frac{\partial \mathbf{U}}{\partial t} dV + \int_{\partial\Omega} (\mathbf{F} - \mathbf{F}_v) n_x dA + \int_{\partial\Omega} (\mathbf{G} - \mathbf{G}_v) n_y dA = \int_\Omega \mathbf{S} dV. \tag{11}$$

At a subsonic inlet boundary, the velocity components and densities are specified, while the normal pressure gradient is set equal to zero. At a subsonic outlet boundary, the ambient pressure is specified, while the normal derivatives of the velocity components and densities are set equal to zero.

Finite Volume Method

With the finite volume method, equation (11) is discretized for each grid cell by approximating

$$\frac{d\mathbf{U}_{i,j}}{dt}Vol_{i,j} + \sum_{s=1}^{N}[(\mathbf{F}-\mathbf{F}_v)n_xA + (\mathbf{G}-\mathbf{G}_v)n_yA]_s = \mathbf{S}_{i,j}Vol_{i,j}. \quad (12)$$

where $\mathbf{U}_{i,j}$ is the volume averaged vector of the conservative variables in the cell $\Omega_{i,j}$ and $\mathbf{S}_{i,j}$ the volume averaged source vector. $Vol_{i,j}$ is the area of the cell. Since we consider structured grids with quadrilaterals as control volumes, the cells have $N = 4$ sides. A_s is the length of the cell interface s. The cell averages $\mathbf{U}_{i,j}$ are the unknowns in the cell-centered finite volume method. Therefore, we have to approximate the flux vectors at the cell interfaces. We shall focus on the approximation of the inviscid flux vectors $\mathbf{F}$ and $\mathbf{G}$. Central discretizations are employed for the viscous fluxes at the cell interfaces. The volume averaged nonlinear source term is approximated by

$$\mathbf{S}_{i,j} \approx \mathbf{S}(\mathbf{U}_{i,j}). \quad (13)$$

After the finite volume discretization of equation (12), we have a system of ODEs for the time dependent cell averages $\mathbf{U}_{i,j}$. We discretize the time derivative in (12) by the explicit Euler method, except for the stiff source term, which is treated by the implicit Euler method. We use the approximate linearization

$$\mathbf{S}_{i,j}^{n+1} \approx \mathbf{S}_{i,j}^{n} + \frac{\partial\mathbf{S}_{i,j}^{n}}{\partial\mathbf{U}'}\Delta\mathbf{U}_{i,j}'^{n}, \quad (14)$$

where superscript n denotes the time level up to which the solution is known, $\mathbf{U}' = (\rho_1, \cdots, \rho_n)^T$ and $\Delta\mathbf{U}_{i,j}'^{n} = \mathbf{U}_{i,j}'^{n+1} - \mathbf{U}_{i,j}'^{n}$. Thus, we employ the semi-implicit scheme

$$\frac{\Delta\mathbf{U}_{i,j}^{n}}{\Delta t} + \frac{1}{Vol_{i,j}}\sum_{s=1}^{N}[(\mathbf{F}^n-\mathbf{F}_v^n)n_xA + (\mathbf{G}^n-\mathbf{G}_v^n)n_yA]_s = \mathbf{S}_{i,j}^{n} + \frac{\partial\mathbf{S}_{i,j}^{n}}{\partial\mathbf{U}'}\Delta\mathbf{U}_{i,j}'^{n}, \quad (15)$$

where Δt is the time step and $\Delta\mathbf{U}_{i,j}^{n} = \mathbf{U}_{i,j}^{n+1} - \mathbf{U}_{i,j}^{n}$ is the change of the cell averaged conservative variables between time levels $n+1$ and n.

1 Rankine-Hugoniot-Riemann Solver

1.1 Review and Outline

Before presenting our new numerical approach to simulate thermoacoustics, we shall briefly review existing methods for computing related problems governed by inhomogeneous conservation laws. When computing stiff reaction waves, the spatial and temporal resolution has to be chosen sufficiently high to avoid non-physical wave speeds. These waves have the structure of a fluid dynamic shock that raises the pressure to some peak value, followed immediately by a reaction zone that brings the pressure back down to a new equilibrium value. On coarse grids it is not possible to resolve this combustion spike and for stiff source terms the numerical wave speed is totally wrong unless the space step is made extremely small. Examples and analyses of the numerical simulation of that problem are given by Oran and Boris [11], LeVeque and Yee [12] , Lindström [13] and Klingenstein [14].

Chorin [15] analyzes the random choice method by Glimm, shows its usefulness for reacting flow and carries out applications in one dimensional time-dependent reacting flow. In this method the solution is first approximated by a piecewise constant function at each time step. It is then advanced in time exactly and new values on the mesh are obtained by sampling. The advantage of this procedure is that the interaction of the flow and the chemical reaction can be taken into account when the Riemann problem is solved.

Roe [16] shows the necessity to modify the upwind schemes for inhomogeneous hyperbolic conservation laws. He approximates the integration along the characteristics taking the source terms into account and shows how to extend such schemes to higher order.

Sweby [17] points out that the TVD (total variation diminishing) property used in high resolution schemes for homogeneous conservation laws is inappropriate for problems with source terms. He utilizes a transformation of dependent variables to reduce the inhomogeneous problem to homogeneous form and suggests to apply the TVD scheme only to the fluxes of the homogeneous system and to treat the source term separately.

Bermudez and Vazquez [18] propose proper upwind discretizations of the source terms (in hydraulics applications). Therefore they introduce a conservation property. In [19] Vazquez extends this method to the 2D shallow water equations.

Instead of increasing the resolution or upwinding the source terms, some authors have proposed flux discretizations, which take the source terms into account. LeVeque et al. [20], [21] developed a scheme where a flux jump at the cell center equals the source term. They show very convincing solutions of the 1D and 2D shallow water equations.

Here, we present a new flux discretization which does not only take into account the source terms but also the viscous terms and multidimensional effects. Our approach was motivated by correcting a non-physical pressure peak and a large mass flow error when computing a steady premixed laminar flame using a conventional Riemann solver. These numerical errors are not related to the ones appearing near contact discontinuities in gas mixture simulations with conservative schemes, if the gases on both sides of the interface have different temperature and different ratios of specific heats γ [22], because the errors in flames also occur, if γ is constant. Since the errors in flames even occur in 1D, they are neither related to similar numerical artifacts at moving shear waves [23]. Considering a simple model equation, we shall see that the numerical problems of conventional Riemann solvers for hyperbolic systems with source terms are caused by discretizing the inviscid fluxes, as if the equations were homogeneous. Most upwind schemes for the compressible Euler and Navier-Stokes equations are based on solving one dimensional Riemann problems at the cell interfaces and make use of conventional homogeneous Riemann solvers. As mentioned above, if such a conventional Riemann solver is applied to compute a steady premixed laminar flame, a non-physical peak in the pressure profile and a large error in the mass flow arise in the results, even if a conservative scheme without source term in the continuity equation is used [24], [4], [5], [6], [7]. These numerical phenomena become much more complex in higher space dimensions and exist also in a weaker form in 1D Navier-Stokes computations due to the viscous terms and in multidimensional homogeneous Euler simulations due to the multidimensional effects. In many flame computations such phenomena are reduced by using fine grids and higher order schemes [25]. Generally these errors are negligible, but if acoustic phenomena in flames are to be simulated, they can become dominant. In spite of the importance only a few people seem to have studied the problems mentioned above and hardly any pressure plots of flames are published, except for [25].

To discretize the equations the cell centered finite volume method is used here. For the time integration the explicit Euler method is applied with an implicit treatment of the source term because of its stiffness. The basic idea of our approach for a flux solver is to transform the volume integrals of the source terms, which also contain the viscous fluxes, into surface integrals. This leads to inhomogeneous Rankine-Hugoniot conditions [9] at the corresponding cell interfaces, because the flux jump corresponds to the source added at a cell interface (Fig. 1 b). If no source is added at the cell interface, homogeneous Rankine-Hugoniot conditions apply (Fig. 1 a). The remaining conditions to determine the states C_1 and C_2 on the left and right sides of a cell interface are provided by linearizing the characteristic relations. Thus, to compute the fluxes and at a cell interface, a non-linear system for six unknowns has to be solved, where three equations come from the linearized Riemann invariants and three from the Rankine-Hugoniot jump conditions. Because of its construction, we call the new inhomogeneous Riemann solver 'Rankine-Hugoniot-Riemann solver', in short 'RHR solver'. If is used as right flux in the left cell and if is used as left flux in the right cell, the source term is properly taken into account in the flux discretization. A steady 1D test case of a premixed laminar flame demonstrates that non-physical pressure peaks and non-constant mass flow profiles can be avoided with this approach. Further it is shown, how the multidimensional effects can be taken into account using the RHR solver. Applying dimension decoupling it is possible to consider the differences of the fluxes in the other space dimensions as parts of the source terms. Thus, the new solver becomes a multidimensional Riemann solver treating the cross fluxes in a physical way using the Rankine-Hugoniot jump conditions. Results of two-dimensional Bunsen flames and of a 2D inviscid channel flow with injection show that the RHR solver leads to much more accurate results than a conventional Riemann solver. Further a 1D simulation of two colliding flames demonstrates that the new solver also works for unsteady flow. Finally a 2D simulation of acoustics flattening a wedge-shaped Bunsen flame to a semicircle shows at least qualitatively a good agreement with experimental measurements. Further details on the derivation, analysis and application of the new approach for a flux solver are presented in the Ph.D thesis of the second author [4].

It is important to mention that combustion is only one application of this approach. The idea is more general and can also be applied to solve other partial differential equations which can be expressed as hyperbolic systems with source terms ex- or including higher spatial derivatives, e.g. the shallow water equations.

In section 1.2, the inhomogeneous Euler and Navier-Stokes equations are presented. The motivation of the present research is described in section 1.3. The Rankine-Hugoniot-Riemann (RHR) solver is outlined and analyzed in section 1.4, while in section 1.5 its extension to multi dimensions is explained. In sections 1.6 and 1.7, results of the RHR solver applied to steady and unsteady 1D and 2D premixed flames are presented and discussed. In section 1.6.2, an application to 2D inviscid non-reacting flow focuses on the multidimensional performance of the RHR solver. Conclusions are stated in section 3.1 of the third part of this lecture.

1.2 Inhomogeneous Euler Equations

For our studies we consider the hyperbolic system of the 2D compressible Euler equations with a source term $\mathbf{S}$:

$$\frac{\partial \mathbf{U}}{\partial t} + \frac{\partial \mathbf{F}}{\partial x} + \frac{\partial \mathbf{G}}{\partial y} \;=\; \mathbf{S}, \tag{16}$$

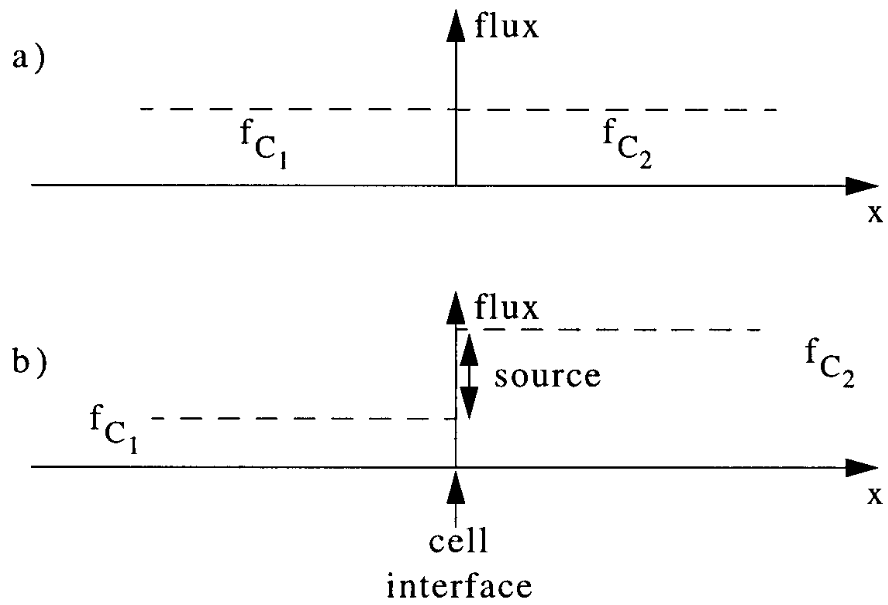

Figure 1: Illustration of Rankine-Hugoniot conditions; a) homogeneous: flux jump equal zero, b) inhomogeneous: flux jump equal source.

where

$$\mathbf{U} = \begin{pmatrix} \rho \\ \rho u \\ \rho v \\ \rho E \end{pmatrix}, \qquad \mathbf{S} = \begin{pmatrix} R \\ M \\ N \\ Q \end{pmatrix}$$

$$\mathbf{F} = \begin{pmatrix} \rho u \\ \rho u^2 + p \\ \rho uv \\ \rho uH \end{pmatrix}, \qquad \mathbf{G} = \begin{pmatrix} \rho v \\ \rho uv \\ \rho v^2 + p \\ \rho vH \end{pmatrix}.$$

$\rho E = \frac{p}{\gamma - 1} + \frac{\rho}{2}(u^2 + v^2)$ is the total energy per unit volume, and $H = \frac{\gamma p}{(\gamma-1)\rho} + \frac{1}{2}(u^2 + v^2)$ is the total enthalpy. R, M, N and Q denote the mass, x- and y-momentum and total energy source rates. In the case of the compressible Navier-Stokes equations, the viscous terms are considered as a part of the source term. For the description of reacting flow, the continuity equation is replaced by the species continuity equations.

Let us consider a steady premixed laminar flame with a simple one-step chemical kinetics model as sketched in Fig. 2. In that model, there are only two species: species A is the reactant, i.e. the unburnt gas, and species B is the product, i.e. the burnt gas. Therefore, we have two species continuity equations for the unburnt and burnt partial densities. The reaction rate k of the one-step mechanism $A \to B$ we used reads in SI units

$$k = 8 \times 10^6 exp(-\frac{7500}{T}) \tag{17}$$

the molecular weights W_A and W_B are $0.029085 kg/mole$, the viscosity μ is $7 \times 10^{-5} Ns/m^2$,

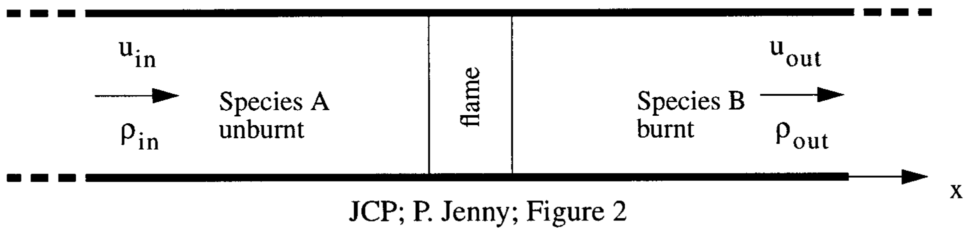

Figure 2: The 1D test case of steady, premixed laminar flame.

the Prandtl and Schmidt numbers are 0.7, the formation enthalpy of species A is zero and $H_B^0 = c_p W_B 1500K$ where $c_p = 1000J/(kgK)$ and $\gamma = 1.4$. γ is the ratio of enthalpy h and internal energy e. If the specific heats c_{p_i} and c_{v_i} are constant as they are here, γ is equal to the ratio of the specific heats of the mixture, i.e. $\gamma = c_p/c_v$. On the cold side of the flame, the unburnt mass fraction is $Y_A = 1$, and the temperature is $T = 300K$.

1.3 Motivation

Our project was motivated by a 1D simulation of a steady premixed laminar flame with very strange results (solid lines in Fig. 3). The simple one-step chemical kinetics model of the previous section 1.2 was used. Since the mass fluxes ρu at inlet and outlet must be equal in the steady-state, we add

$$\frac{\rho_{out} u_{out} - \rho_{in} u_{in}}{\rho_{in} - \rho_{out}} \tag{18}$$

to the velocity field after each time step. Thereby, the mass conservation is enforced, and the flame is forced to stay within the computational domain. At the outlet, the pressure is set equal to $10^5 Pa$.

We used an explicit cell centered finite volume method to solve this system with a point implicit treatment of the source term (15). The viscous terms are second-order centrally discretized.

Although a conservative scheme was applied without source term in the global continuity equation, the mass flow profile of the steady state result (solid lines in Fig. 3) shows a gap in the region of the reaction zone. We shall see that the huge unphysical peak in the pressure profile has the same origin.

For the simulation of the 1D steady premixed laminar flame, the characteristic based approximate Riemann solver [26], [27], [28] was used to compute the 1D flux $\mathbf{F}$ at the cell interfaces. Although the present problem is governed by inhomogeneous equations with important source terms, a conventional Riemann solver like our characteristic based one numerically solves the homogeneous 1D Euler equations.

The characteristic based approximate Riemann solver is based on the idea of solving 1D shock tube problems at each cell interface at each time step. With the assumptions above one has the characteristic relations

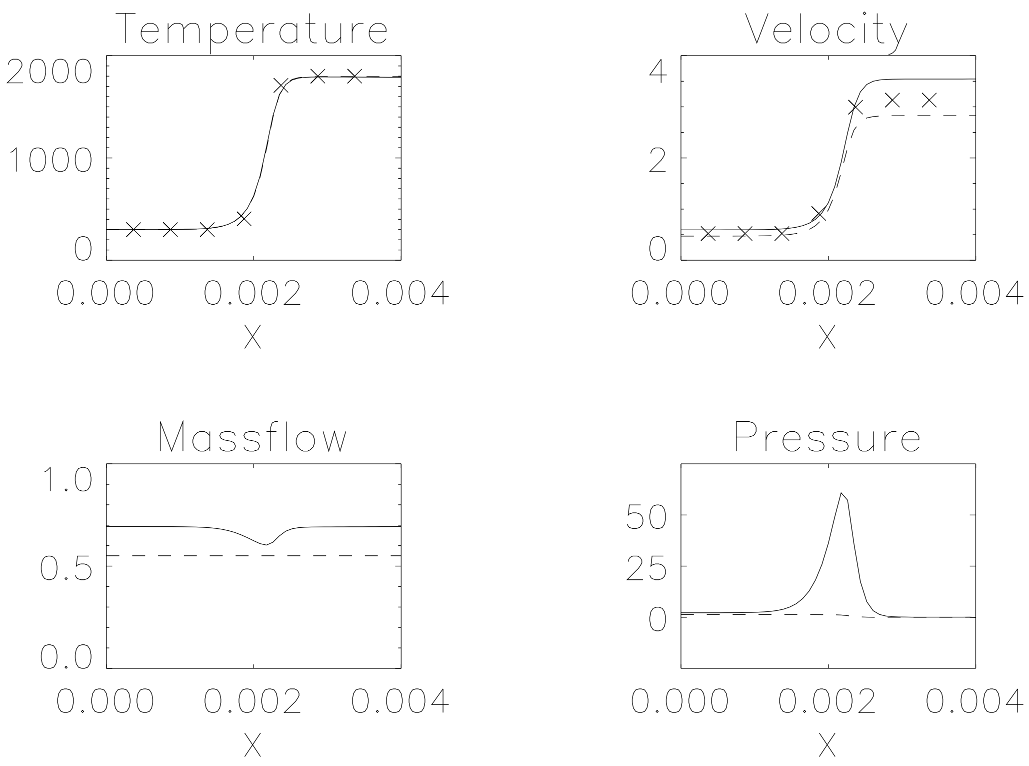

Figure 3: 1D test case of steady, premixed laminar flame: conventional Riemann solver (solid lines); RHR solver (dashed lines); reference solution (markers).

$$\begin{array}{rcrcll} dp & - & \rho c du & = & 0 & \text{along } \frac{dx}{dt} = u - c \\ dp & - & c^2 d\rho & = & 0 & \text{along } \frac{dx}{dt} = u \\ dp & + & \rho c du & = & 0 & \text{along } \frac{dx}{dt} = u + c \end{array} \qquad (19)$$

assuming that the Riemann invariants remain unchanged when the corresponding characteristics cross a shock (Fig. 4).

That assumption is well justified for low Mach number flow considered here. The discretization and linearization of the characteristic relations (19) leads to three linear algebraic equations (20) for the state at the cell interface which determines the fluxes (region $C = C_1 \cup C_2$ in Fig. 6). We assume $u_C > 0$.

$$\begin{array}{rcllcl} (p_C - p_B) & - & \rho_B c_B & (u_C - u_B) & = & 0 \\ (p_C - p_A) & - & c_A^2 & (\rho_C - \rho_A) & = & 0 \ , \\ (p_C - p_A) & + & \rho_A c_A & (u_C - u_A) & = & 0 \end{array} \qquad (20)$$

But with a source term in one of the neighboring cells the assumption of having 1D shock tube problems at the cell interfaces and therefore of having Riemann invariants along the characteristics is wrong. It turned out that this is the reason for the numerical errors of the characteristic based approximate Riemann solver, i.e. $\mathbf{f}(\mathbf{U}_C)$ with $\mathbf{U}_C$ determined by (20), in Fig. 3. Employing Roe's approximate Riemann solver instead of the characteristic based one gave almost the same poor results.

The dashed lines in Fig. 3 represent the result obtained with our new flux solver which is explained next.

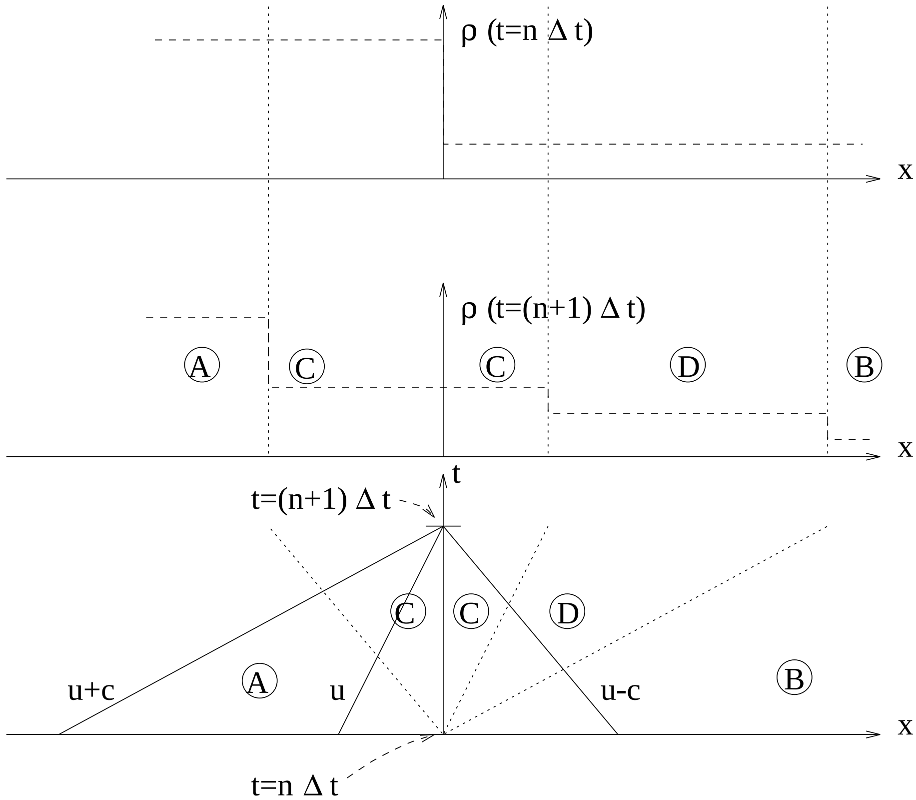

Figure 4: Characteristic based approximate Riemann solver.

1.4 Rankine-Hugoniot-Riemann(RHR) Solver

The basic idea for our approach is to treat the source terms as surface integrals instead of volume integrals. The parameter α_i in Fig. 5 is the fraction of the source terms in cell i distributed to the left interface ($0 \leq \alpha_i \leq 1$).

Thus, one obtains piecewise homogeneous hyperbolic conditions in 1D with source term discontinuities at the cell interfaces which would be located in the area C in Fig. 4. Since the rate of mass, momentum and energy added at a cell interface induces a flux jump (cf. Fig. 1 b), it is necessary to divide C into regions C_1 and C_2 in Fig.6. During one time step constant states are assumed within the areas A, B, C_1 and C_2. Therefore, to fulfill the Rankine-Hugoniot jump conditions, the difference between the fluxes in C_1 and C_2 must be equal to the corresponding source term discontinuities:

$$\begin{array}{rl} (\rho u)_{C_2} - (\rho u)_{C_1} & = \Delta x R_{i-1/2} \\ (\rho u^2 + p)_{C_2} - (\rho u^2 + p)_{C_1} & = \Delta x M_{i-1/2} \\ (\rho u H)_{C_2} - (\rho u H)_{C_1} & = \Delta x Q_{i-1/2} \end{array} \tag{21}$$

where $\mathbf{S}_{i-1/2} = \alpha_i \mathbf{S}_i + (1 - \alpha_{i-1})\mathbf{S}_{i-1}$ with $\mathbf{S} = (R, M, Q)^T$. Since the conditions are homogeneous and hyperbolic within the cells on both sides of the interface, one obtains the following linearized Riemann invariants:

$$\begin{array}{rcccl} (p_{C_2} - p_B) & - & \rho_B c_B & (u_{C_2} - u_B) & = 0 \\ (p_{C_1} - p_A) & - & c_A^2 & (\rho_{C_1} - \rho_A) & = 0 \\ (p_{C_1} - p_A) & + & \rho_A c_A & (u_{C_1} - u_A) & = 0 \end{array} \tag{22}$$

The equations (21) and (22) form a nonlinear algebraic system for ρ, u and p in the areas C_1 and C_2. Applying the Newton-Raphson method and using good start values (for

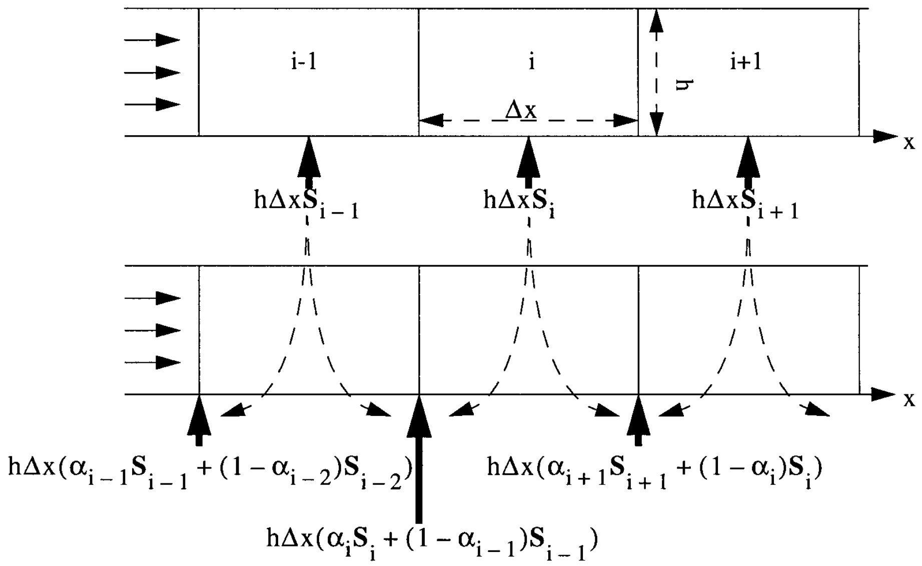

Figure 5: Source terms distributed to cell interfaces.

example those from the left and right cells at the time $t = n\Delta t$), one or two iterations are usually enough.

It is important to notice that it is not necessary to store both fluxes $(\mathbf{F}_{C_1})_{i-1/2}$ and $(\mathbf{F}_{C_2})_{i-1/2}$. The time stepping, e.g. using explicit Euler

$$\mathbf{U}_i^{n+1} = \mathbf{U}_i^n + \Delta t \left(\frac{\mathbf{F}_{i-1/2}^n - \mathbf{F}_{i+1/2}^n}{\Delta x} + \mathbf{S}_i^n \right) \tag{23}$$

can be done in the same way as with any other flux solver if one uses either

$$\mathbf{F}_{i-1/2}^n = (\mathbf{F}_{C_1})_{i-1/2} + \Delta x (1 - \alpha_{i-1}) \mathbf{S}_{i-1} \tag{24}$$

or

$$\mathbf{F}_{i-1/2}^n = (\mathbf{F}_{C_2})_{i-1/2} - \Delta x \alpha_i \mathbf{S}_i \tag{25}$$

The superscript n means that the values are taken at the time $t = n\Delta t$.

1.4.1 Accuracy of the Inviscid Terms in the Steady-State

We assume that in 1D the integral over the source terms (and viscous terms) in cell i is accurate of order Δx^k, i.e. the error is $\beta_i \Delta x^k$. We define

$$\langle \beta \rangle = \tfrac{1}{N} \textstyle\sum_{j=1}^{N} \beta_j \quad \text{and} \quad \Delta x = \tfrac{L}{N} \tag{26}$$

where L is a constant length scale and N is the number of cells. In the steady-state the difference of the fluxes at $x_{i+1/2}$ and $x_{i-1/2}$ must be equal to the integral over the source term in cell i due to the conservativity of the scheme. Therefore, if the flux at $x_{1/2}$ is exact (e.g. if we have Dirichlet boundary conditions), the error of the flux at $x_{3/2}$ is $\beta_1 \Delta x^k$. At $x_{N+1/2}$ the expected error is

$$\Delta x^k N \langle \beta \rangle = \Delta x^k \tfrac{L}{\Delta x} \langle \beta \rangle = \Delta x^{k-1} L \langle \beta \rangle. \tag{27}$$

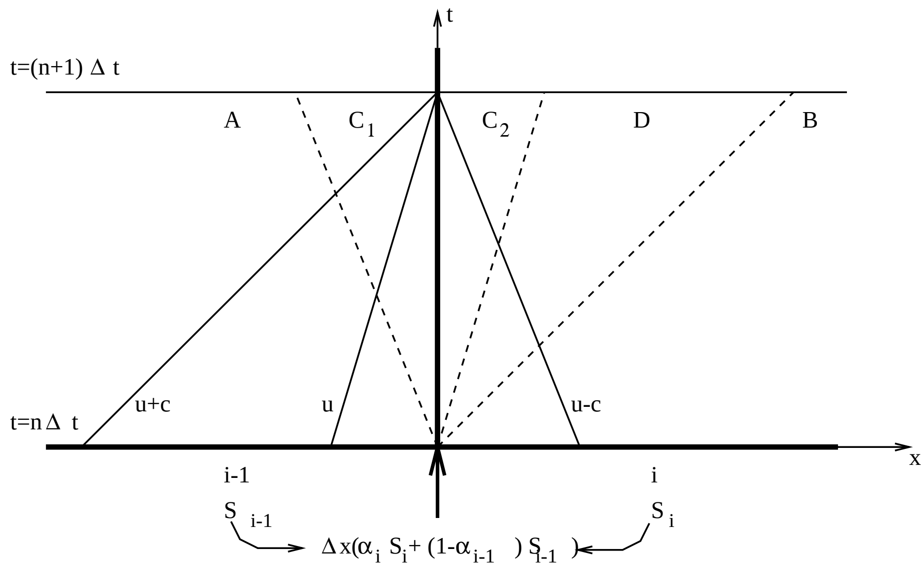

Figure 6: Rankine-Hugoniot-Riemann solver.

Since in the steady-state the fluxes at the interface $x_{i+1/2}$ are equal to those in cell i if the RHR solver with $\alpha_i = 1$ is applied, the differences between the numerical steady-state fluxes in cell i and the exact fluxes at $x_{i+1/2}$ are of order Δx^{k-1}. This has been demonstrated with a 1D Euler test case with a source term $Q(x)$ in the energy equation (Fig. 7; $Q(x)$ in units of $2.5 \times 10^5 kg/(ms^3)$, $R = M = 0$). The source term is a known function of x and can be exactly integrated over each cell. At the left boundary the velocity is $50m/s$ and the temperature is $300K$. At the right boundary the pressure is $10^5 Pa$. In figure 7 the velocity profiles of the steady-state solutions obtained on grids with 5, 10, 20 and 40 cells are shown. It can be observed that the cell averaged values are identical to the exact ones at the corresponding right cell interfaces.
For $0 \leq \alpha \leq 1$ the RHR solver guarantees that the fluxes in cell i lie between those at the corresponding interfaces, if the source term components do not change their sign within the cells i, $i+1$ and $i-1$. Therefore the fluxes in the cells are bounded by the fluxes at the interfaces. This is not the case with a conventional Riemann solver.

1.4.2 RHR Solver for Inhomogeneous Linear Hyperbolic Systems

Let us consider the linear hyperbolic system with source term $\mathbf{S}(\mathbf{U})$

$$\frac{\partial \mathbf{U}}{\partial t} + \mathbf{A}\frac{\partial \mathbf{U}}{\partial x} = \mathbf{S}(\mathbf{U}), \tag{28}$$

where $\mathbf{A}$ is a nonsingular, constant and diagonalizable matrix, i.e. $\mathbf{A} = \mathbf{R}\mathbf{\Lambda}\mathbf{R}^{-1}$. The diagonal matrix $\mathbf{\Lambda} = diag(\lambda_i)$ contains the eigenvalues λ_i of $\mathbf{A}$. Application of the RHR solver at the cell interface $x_{i-1/2}$ yields the Rankine-Hugoniot conditions

$$(\mathbf{A}\mathbf{U}_{C_2})^n_{i-1/2} - (\mathbf{A}\mathbf{U}_{C_1})^n_{i-1/2} = \Delta x \mathbf{S}^n_{i-1/2} \tag{29}$$

Since the components of $\mathbf{R}^{-1}\mathbf{U}$ are Riemann invariants and determined by their upstream values, we obtain for the positive and negative flux contributions at the left and right sides of the cell interface, respectively:

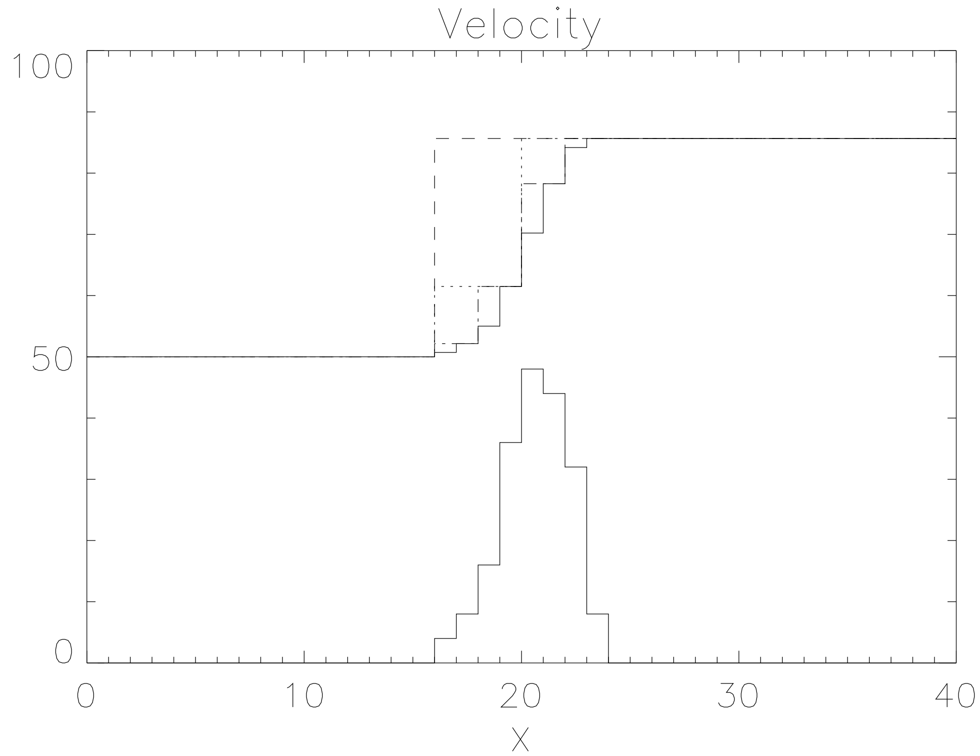

Figure 7: Velocity plot of a 1D Euler test case with an exact source term (lower plot; $Q(x)$ in units of $2.5 \times 10^5 kg/(ms^3)$) in the energy equation on 4 different grids; 5, 10, 20, 40 cells: dashed, dotted, dash-dotted, solid lines.

$$\begin{aligned} (\mathbf{A}^+\mathbf{U}_{C_1})^n_{i-1/2} &= \mathbf{A}^+\mathbf{U}^n_{i-1}, \\ (\mathbf{A}^-\mathbf{U}_{C_2})^n_{i-1/2} &= \mathbf{A}^-\mathbf{U}^n_i, \end{aligned} \tag{30}$$

where $\mathbf{A}^\pm = \mathbf{R}\mathbf{\Lambda}^\pm\mathbf{R}^{-1}$ with $\mathbf{\Lambda}^+ = diag(max(\lambda_i, 0))$ and $\mathbf{\Lambda}^- = diag(min(\lambda_i, 0))$. Using $\mathbf{A} = \mathbf{A}^+ + \mathbf{A}^-$ and the relations (30) and (29), we get for the RHR flux at the left cell interface

$$(\mathbf{A}\mathbf{U}_{C_2})^n_{i-1/2} = \mathbf{A}^-\mathbf{U}^n_i + \mathbf{A}^+\mathbf{U}^n_{i-1} + \mathbf{A}^+\mathbf{A}^{-1}\Delta x\mathbf{S}^n_{i-1/2} \tag{31}$$

With similar arguments, we obtain the RHR flux at the right cell interface. Thus, the RHR solver for the inhomogeneous linear hyperbolic problem reads:

$$\mathbf{U}^{n+1}_i = \mathbf{U}^n_i - \frac{\Delta t}{\Delta x}[\mathbf{A}^+(\mathbf{U}^n_i - \mathbf{U}^n_{i-1}) + \mathbf{A}^-(\mathbf{U}^n_{i+1} - \mathbf{U}^n_i)] + \Delta t[\mathbf{A}^+\mathbf{A}^{-1}\mathbf{S}^n_{i-1/2} + \mathbf{A}^-\mathbf{A}^{-1}\mathbf{S}^n_{i+1/2}] \tag{32}$$

In the steady-state, the upwind and downwind flux differences are exactly balanced by the upwind and downwind projected source integrals, respectively. Thus, the Rankine-Hugoniot conditions

$$\mathbf{A}\mathbf{U}_i - \mathbf{A}\mathbf{U}_{i-1} = \Delta x\mathbf{S}_{i-1/2} \tag{33}$$

are indeed satisfied, contrary to a conventional upwind scheme. For $\alpha = 1/2$, the RHR solver coincides with LeVeque's extension of Godunov's scheme (cf. [20] for a similar analysis) and Roe's source term treatment [16]. However, those approaches differ from the RHR solver in the nonlinear case.

1.5 Extension to Multi Dimensions

The extension to multi dimensions is based on the fact that a multi dimensional system is equivalent to an infinite number of independent 1D systems in one coordinate direction, if the flux derivatives in the other coordinate directions are known and considered as a part of the source term. Of course, this is not a realistic situation, but in the finite volume case we can use the fluxes at the cell interfaces at the old time level to approximate the flux derivatives and to modify the source terms.

For simplicity a Cartesian 2D grid is used for the following investigations. It will be shown that it is possible to treat each row and each column of the grid in Fig. 8 as a 1D problem, if the approximation of the cross flow fluxes is good enough. The governing equations are the inhomogeneous Euler equations (16).

We use the fluxes in the y-direction to approximate $\partial\mathbf{G}/\partial y$ and to modify the source term $\mathbf{S}$:

$$\mathbf{S}^{\star}_{i,j} = \mathbf{S}_{i,j} + \frac{\mathbf{G}_{i,j-1/2} - \mathbf{G}_{i,j+1/2}}{\Delta y}. \tag{34}$$

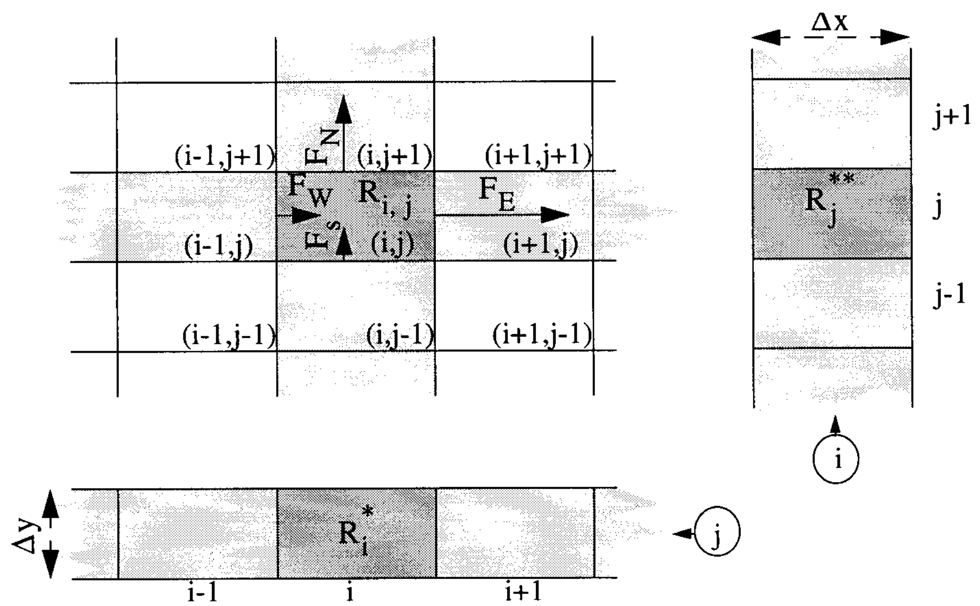

Figure 8: Cross flow fluxes as source terms.

With this modified source term we obtain 1D problems for each grid line. If the Navier-Stokes equations are solved, the source terms $\mathbf{S}_{i,j}$ also contain the viscous flux balance. Now we can apply the RHR solver to compute the inviscid fluxes at the eastern and western cell interfaces. We use equations (21), (22) together with the Rankine-Hugoniot equation for the cross flow flux, i.e. $(\rho uv)_{C_2} - (\rho uv)_{C_1} = \Delta x N_{i-1/2}$, and the characteristic relation $dv = 0$ along $\frac{dx}{dt} = u$, i.e. $v_{C_1} - v_A = 0$, if u is positive. When the nonlinear system for $(\rho, u, v, p)^T$ in the regions C_1 and C_2 is solved, the flux $\mathbf{F}_{i-1/2}$ can be determined according to (24) or (25). The mass fraction of a species k is determined by the characteristic relation $dY_k = 0$ along $\frac{dx}{dt} = u$, i.e. $Y_{k\,C_1} - Y_{k\,A} = 0$, if u is positive. Then the species mass flux $(\rho u Y_k)_{i-1/2}$ is computed by applying (24).

The computation of the fluxes at the northern and southern interfaces is analogous:

$$\mathbf{S}^{\star\star}_{i,j} = \mathbf{S}_{i,j} + \frac{\mathbf{F}_{i-1/2,j} - \mathbf{F}_{i+1/2,j}}{\Delta x} \tag{35}$$

For the first time step, 10 iterations are made starting with the fluxes obtained with a conventional Riemann solver.

In short one can describe the whole procedure as follows:

(i) The source terms have to be modified using (34) with the fluxes of the old time step. Note that $\mathbf{S}_{i,j}$ contains the viscous terms as well.

(ii) Because of stability reasons [5], the modification $\bar{\mathbf{S}}^{\star}_{i,j} = (1-\theta)\mathbf{S}^{\star}_{i,j} + \frac{\theta}{4}(\mathbf{S}^{\star}_{i+1,j} + \mathbf{S}^{\star}_{i-1,j} + \mathbf{S}^{\star}{}_{i,j+1} + \mathbf{S}^{\star}_{i,j-1})$ for the source terms is suggested. We have used $\theta = 0.04$ which is an empirical value.

(iii) Using $\bar{\mathbf{S}}^{\star}_{i,j}$, the RHR solver can be applied to derive the fluxes at the eastern and western cell interfaces. We have chosen $\alpha_{i,j}$ equal to one, if u was positive at the interfaces $\partial\Omega_{i\pm1/2,j}$ and equal to zero , if u was negative at both interfaces. For $u_{i+1/2,j}u_{i-1/2,j} \leq 0$, α was set equal to $u_{i-1/2,j}/(u_{i-1/2,j} - u_{i+1/2,j})$, if not both $u_{i-1/2,j}$ and $u_{i+1/2,j}$ were zero. In that case $\bar{\mathbf{S}}^{\star}_{i,j}$ was set equal to zero, since then the RHR solver needs not to be applied.

(iv) Analogously to (i), (ii) and (iii), the northern and southern fluxes can be determined.

(v) These fluxes and the source term $\mathbf{S}_{i,j}$ are used for the time integration.

(vi) Goto (i) for next time step.

Modifications of the source terms are necessary to extend the RHR solver to axisymmetric flow with or without swirl, to flow in a rotating frame of reference, to 3D and to structured grids with curvilinear coordinates.

We have seen that the RHR solver fully takes into account the source terms, whatever they contain. In this case they contain the 2D effects and therefore, opposed to other flux solvers, the RHR solver allows to make a physically based dimension decoupling. Thus, the RHR solver is a multidimensional Riemann solver.

1.6 Results for Steady Flow

The Rankine-Hugoniot-Riemann (RHR) solver is applied to steady low Mach number flow with and without combustion. The RHR results for 1D and 2D premixed laminar flames (sections 1.6.1 and 1.6.3, respectively) and a 2D inviscid channel flow (section 1.6.2) are shown to be much more accurate than the results obtained with a conventional Riemann solver.

1.6.1 1D Premixed Laminar Flame

The dashed lines in Fig. 3 show the steady-state results (40 cells) obtained with the RHR solver with $\alpha_i = 0.5$ for the 1D flame test case introduced in section 1.3. The solid lines in Fig. 3 show the steady-state results obtained with the characteristic based Riemann solver. The temperature profiles are almost the same, but with the RHR solver the mass flux is constant (dashed lines of Fig. 3), there is no pressure peak and the laminar flame speed is closer to the reference value which is about $0.522m/s$ obtained with an unsteady flame simulation on a fine grid. It can be seen that the RHR solver leads to much more accurate 1D steady-state results than a conventional Riemann solver. The correct pressure distribution obtained with the RHR solver is enlarged in Fig. 9. Although the RHR solver is second-order accurate for $\alpha = 0.5$ (and first-order accurate for $\alpha \neq 0.5$), grid refinement indicates that the flame velocity in this test case is only first-order accurate. In section 1.6.3, the RHR solver is applied to a 2D premixed laminar flame.

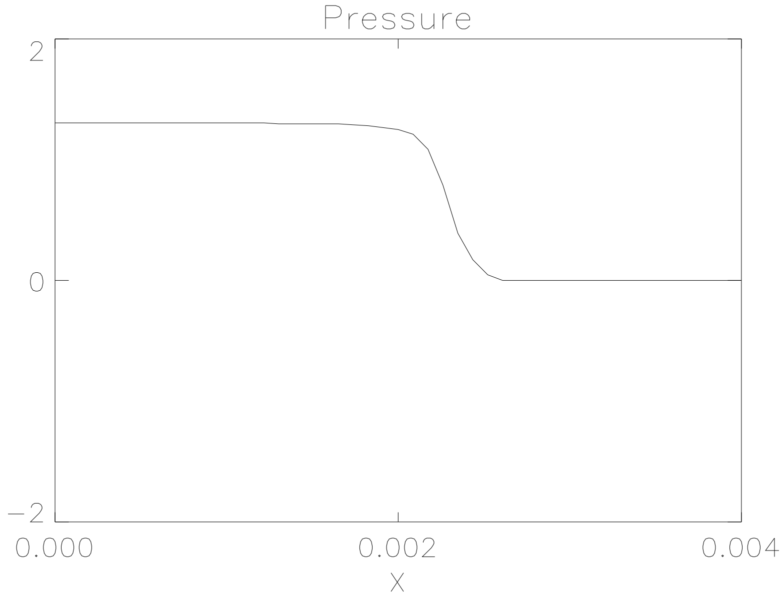

Figure 9: 1D test case of steady, premixed laminar flame; $p - p_{out}$ with RHR solver.

1.6.2 Injection in 2D Inviscid Channel Flow

This test case will demonstrate that the RHR solver can lead to significant better results than a conventional upwind scheme even if the 2D Euler equations without source term are solved, since in general the modified source terms are non zero due to the multidimensional effects.

To test our scheme for the homogeneous compressible 2D Euler equations a channel flow with injection from both sides is investigated (Fig. 10).

Since the maximum Mach number is very low, the total pressure $p_{tot} = p + (u^2 + v^2)\rho/2$ has to be approximately constant along each streamline in the steady-state. The bottom plot of Fig. 11 shows that this is fulfilled very well, if the RHR solver is used (a 16×16 grid was used for one symmetry half). However, the result obtained with a conventional Riemann solver contains non-physical pressure peaks (top plot of Fig. 11) due to neglecting the 2D effects.

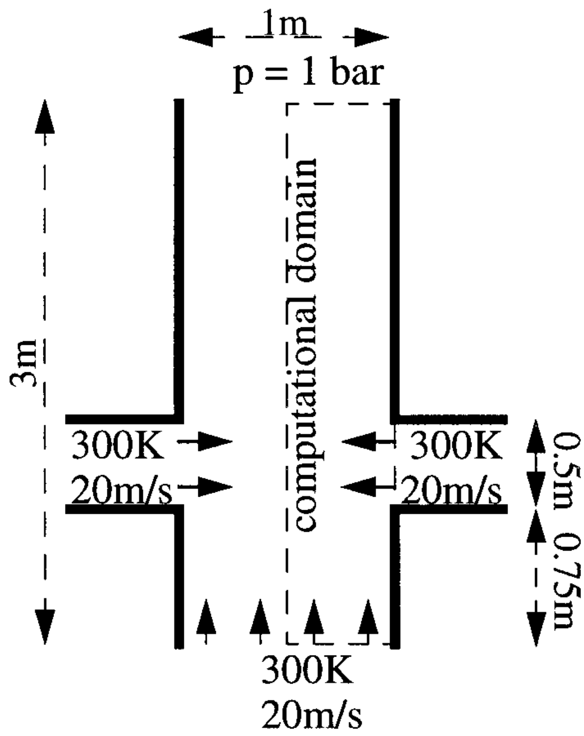

Figure 10: The 2D Euler test case without source terms; injection in channel flow.

1.6.3 Laminar Bunsen Flame

The differences in the pressure field become even more dramatic if a source term is involved. A 2D test case of an infinite series of steady laminar Bunsen flames was investigated (Fig. 12). The same one step mechanism (17) of the 1D flame in Fig. 3 and a 16×21 grid (for one symmetry half) were used and the velocity at the nozzle exit was $2m/s$. Although the numerical flame shapes are similar and correspond very well to the approximate analytical solution of the flame contour, there are huge differences between the two pressure fields $p - p_{out}$ (Fig. 13). While the results obtained with a conventional Riemann solver (top plot of Fig. 13) show pressure differences of about $150Pa$ (especially if acoustics in flames is to be studied such huge errors will corrupt the results) the results obtained with the RHR solver show pressure differences of only $12Pa$ (bottom plot of Fig. 13). The pressure decrease of about $2Pa$ across the flame corresponds precisely to the theoretical expectation and to the results of the 1D test case.

1.7 Results for Unsteady Flow

The Rankine-Hugoniot-Riemann (RHR) solver is applied to simulate acoustic effects in low speed combustion. The results for the sound generation by colliding 1D flames (section 1.7.1) are shown to be in excellent agreement with an analytical solution. In section 1.7.2, the interaction of oscillating acoustic waves with a 2D Bunsen flame is computed.

1.7.1 Sound Generation by Colliding Flames

The following 1D test case suggested by Prof. G. Searby, IRPHE-CNRS, Marseille, shall demonstrate that the RHR solver allows to make numerical studies of acoustics produced

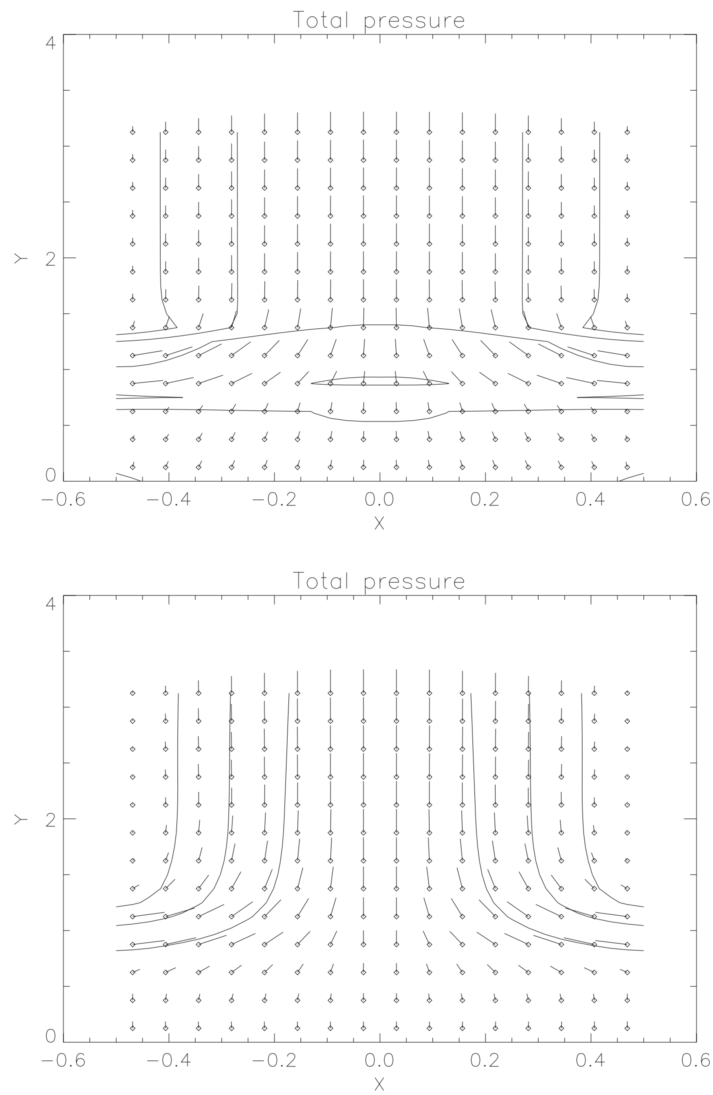

Figure 11: 2D Euler test case without source terms; total pressure contours and velocity fields: conventional Riemann solver (top); RHR solver (bottom).

by two colliding flames in a tube. The same flame as in Fig. 3 has been used but due to stability problems with $\alpha = 0.5$ the source term has been distributed to the upwind side of the cell (for positive velocities to the left else to the right cell interface).

The collision of two flames in an infinitely long tube is studied. As the gradients at the boundary are assumed to be small, Neumann boundary conditions have been applied on $\mathbf{U}$ in order to have no reflections. The computational domain is the part of the tube where the collision of the flames takes place and is $2mm$ long (only one half of the symmetric field). The grid has 25 grid points and the time step was $8 \times 10^{-8} s$ (the maximum Courant number was about 0.8). In Fig. 14, the flames before the collision are sketched. They do not interfere yet, and the states in the areas on the left and right sides of the flames and between them are constant.

After the collision (sketched in Fig. 15), two expansion waves travel away from the center with a constant speed u_{wave}, and the fluid between them is at rest. As the states at infinity are known and constant states can be assumed in the areas between and outside the waves, we have the possibility to figure out the wave velocity u_{wave} as well as the

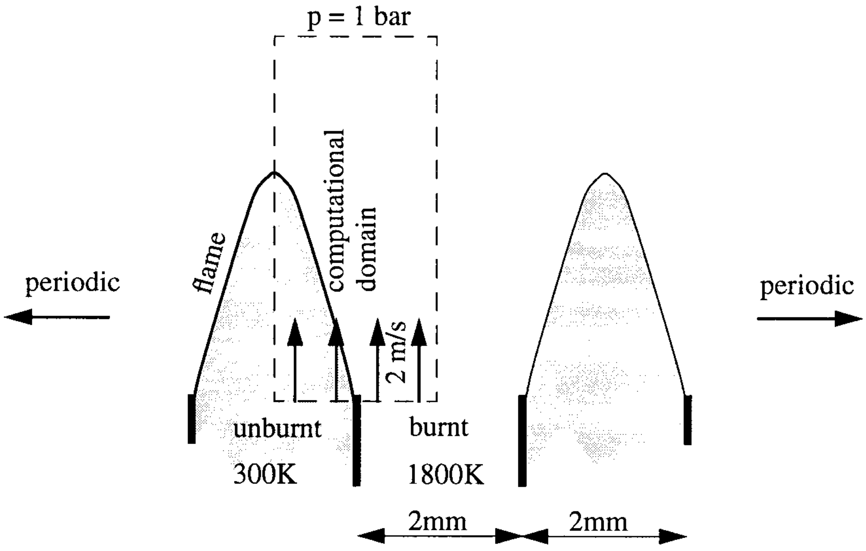

Figure 12: The 2D combustion test case; an infinite series of Bunsen flames.

pressure and temperature in the center p_{center} and T_{center} with the three Rankine-Hugoniot relations, if we approximate the expansion wave by a discontinuity. The derivation is given by Jenny [4].

The values at the outflow boundary at $t = 0s$ in our simulation are $u_{out} = 2.85611 m/s$ and $T_{burnt} = 1795.57K$. We have $p_\infty = 10^5 Pa$, $\gamma = 1.4$ and $c_p = 10^3 (m/s)^2/K$. With these data, the analytical solution [4] yields $u_{wave} = 848.63 m/s$, $T_{center} = 1793.15K$ and $p_{center} - p_\infty = -470.86 Pa$. The acoustic wave speed $u_{wave} = u + c$ is slightly larger than the speed of sound in the burnt gas which is $c_{burnt} = \sqrt{(\gamma - 1)c_p T} = 847.48 m/s$.

With this we have a good estimate of the values in the center after the collision. To say more about the pressure during the collision, the linear dependence of the acoustic pressure $p - p_\infty$ on $\dot{q}$, the rate of heat released in the domain [2] is investigated. Thus, we check the dependence

$$p - p_\infty \approx c_1 \dot{q} + c_2, \tag{36}$$

at the center. c_1 and c_2 in (36) are constants.

At the beginning, the pressure at the center p_{center} and the net rate of heat released $\dot{q}$ are constant. As soon as the preheat zones of the two flames interfere, the reaction rate and the net heat release rate $\dot{q}$ grow and therefore the pressure level increases. After a while, $\dot{q}$ becomes smaller because there is less and less fuel left until it is consumed at all. Then, $\dot{q}$ is zero, and the pressure at the center p_{center} remains constant.

Fig. 16 shows the temperature, the velocity and the mass fraction of the product at three different times. In Fig. 17, the acoustic pressure profiles at four different times are presented.

To show that the simulation fulfills the criterion (36) at the center not only at the $t = 0$ and $t \to \infty$, $p_{center} - p_\infty$ and $c_1 \dot{q} + c_2$ with appropriate constants

$$c_1 = (p_{center}(t=0) - p_{center}(t \to \infty))/\dot{q}(t=0), \qquad c_2 = p_{center}(t \to \infty) - p_\infty$$

are plotted as a function of time in Fig. 18. As expected one can see only one curve.

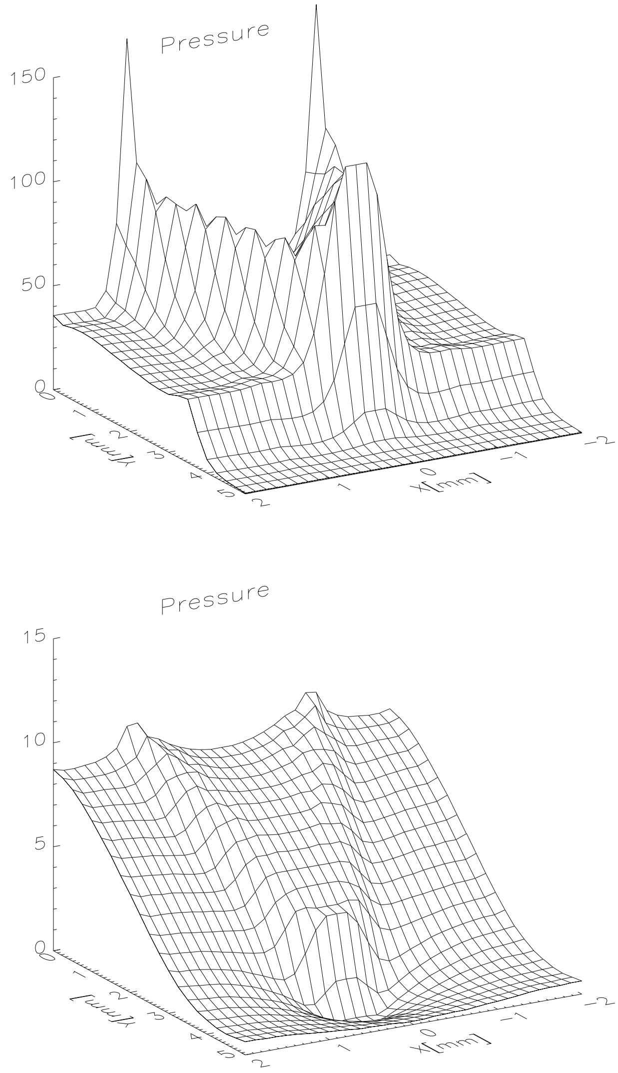

Figure 13: 2D combustion test case; pressure surface plots: conventional Riemann solver (top); RHR solver (bottom).

The difference is shown in Fig. 19. The numerical values at the center at the end of this simulation are $1793.11K$ for the temperature (analytical: $T_{center} = 1793.15K$) and $-471.17Pa$ for the acoustic pressure (analytical: $p_{center} - p_{\infty} = -470.86Pa$). The velocity is zero as it should be. Thus, the numerical results correspond almost precisely to the analytical ones.

1.7.2 Oscillating Bunsen Flame

The purpose of the following test case, suggested by Prof. G. Searby, IRPHE-CNRS, Marseille, [29] and sketched in Fig. 20, was to check the ability of our scheme to deal with unsteady 2D flow simulations.

The initial state was the steady Bunsen flame of section 1.6.3, but with farfield boundary conditions. The velocity of the cold gas mixture at the outlet of the tube was $1.5m/s$ and it started to oscillate at the time $t = 0s$ with $10000Hz$ and with an amplitude of $1m/s$. Experiments by Hahnemann et al. [30] use a strong sound source located downstream

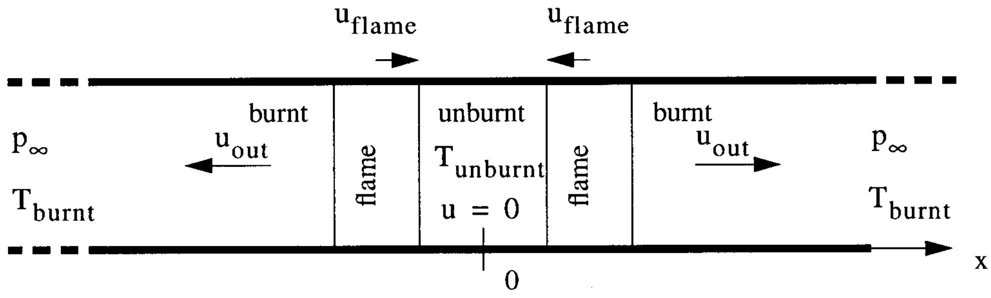

Figure 14: Test of two colliding flames generating sound; before the collision.

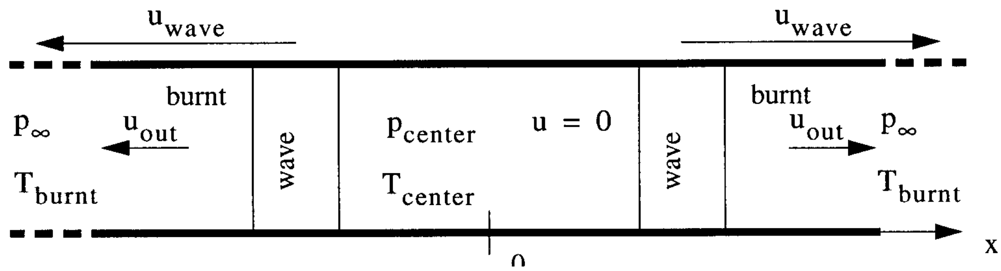

Figure 15: Test of two colliding flames generating sound; after the collision.

in the tube and their measurements show that the flame contours tend to be close to sound potential surfaces [31]. Figure 21 shows unburnt mass fraction isolines and velocity fields of our simulation at the times $0.014025s$, $0.014050s$, $0.014075s$ and $0.014100s$ in the same plot (the isolines of the results at $t = 0.0141s$ are solid while the others are dotted). Additionally the isolines of the analytical solution of the sound potential surfaces [31] are shown (dashed lines) and like in Hahnemann et al.'s axisymmetric experiments one can see that the flame contours are close to one of those surfaces. Fig. 22 shows the pressure at the tube outlet $x = 0$ at the center $y = 0$ as a function of time after 140 oscillations. The difference between the maximum and the minimum pressure is about $150Pa$ which is almost equal to the pressure error peak in the steady-state results of the same flame with a conventional upwind scheme (figure 13).

For this simulation a grid of 16×21 points (for one symmetry half) was used. One oscillation cycle took approximately 1 hour on a SUN SPARC 20 workstation without any attempt to optimize the code. The flame was already flattened after about 5 oscillation cycles.

2 Convergence Acceleration for Low Speed Combustion

2.1 Review and Outline

The convergence of compressible low Mach number flow computations can be accelerated to steady-state by using an implicit scheme with a less stringent time step restriction [32] or by using a multigrid method. Volpe [33] employed both techniques to compute steady flow over a circular cylinder at the freestream Mach numbers $M_\infty = 0.1, \quad 0.01, \quad 0.001$. However, convergence and accuracy problems were encountered with these conventional

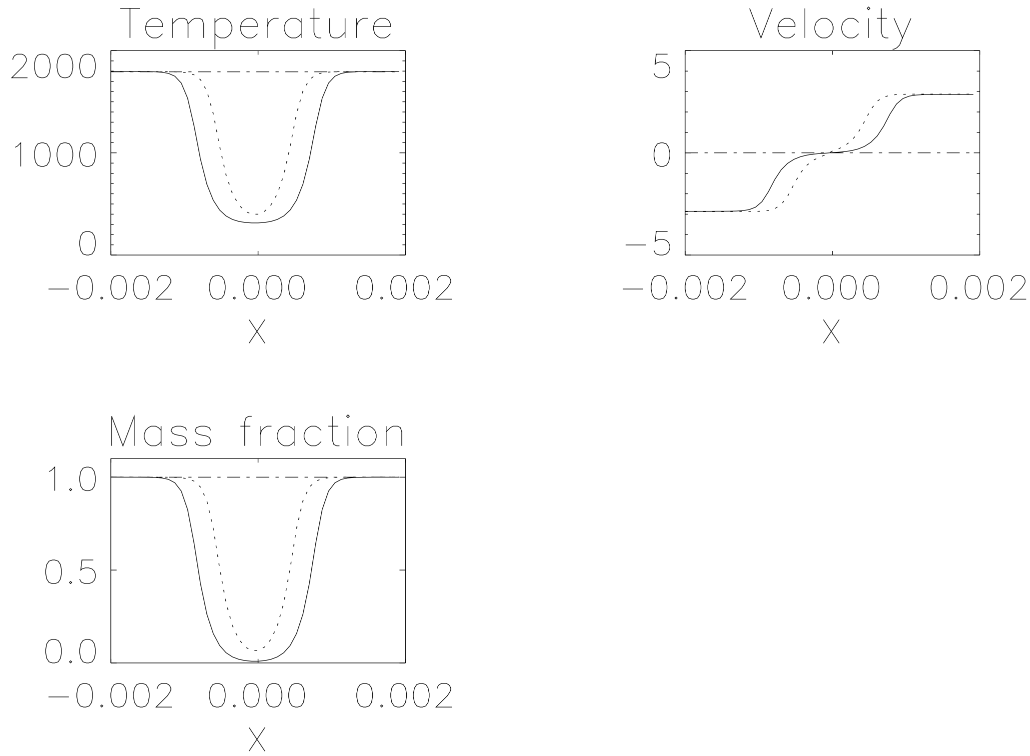

Figure 16: Sound generation by colliding flames; temperature, velocity and mass fraction at three different times, $t = 0$: solid line, $t = 5 \times 10^{-4}s$: dotted line, $t = 10^{-3}s$: dashed dotted line.

approaches for $M_\infty \to 0$.

Ramshaw and Mousseau [34] show a way of artificially reducing the speed of sound to values comparable to the flow velocity by introducing a modified equation of state. Therefore, they solve an extra evolution equation such that the correct equation of state is fulfilled in the steady-state. It is easy to implement this method in explicit compressible Euler codes, but extra boundary conditions are required and the method does not work for unsteady flow.

O'Rourke and Bracco [35] introduce a transformation, which is associated with the spatial uniformity of the time-varying pressure and is shown to be valid for low Mach number flows. It reduces the computational time by reducing the total number of time steps.

In recent years, considerable progress has been made in the development of time derivative preconditioning methods for accelerating the steady-state convergence of Euler and Navier-Stokes solvers at low Mach numbers [36], [37], [38]. An excellent review is given by Turkel [39]. The recent developments are treated by other lecturers at this "30th Computational Fluid Dynamics" VKI Lecture Series.

By multiplying the time derivative with an appropriate local positive definite matrix, the ratio of the wave speeds of the hyperbolic system is changed from $O(M^{-1})$ with the Euler equations to $O(1)$ for the modified equations, where M denotes the local Mach number. If the preconditioned system is also accounted for by the spatial discretization of the numerical dissipation, the loss of accuracy at low Mach numbers can be avoided [38]. For low cell Reynolds numbers ($Re_{\Delta x} < 1$), viscous effects can be incorporated into the

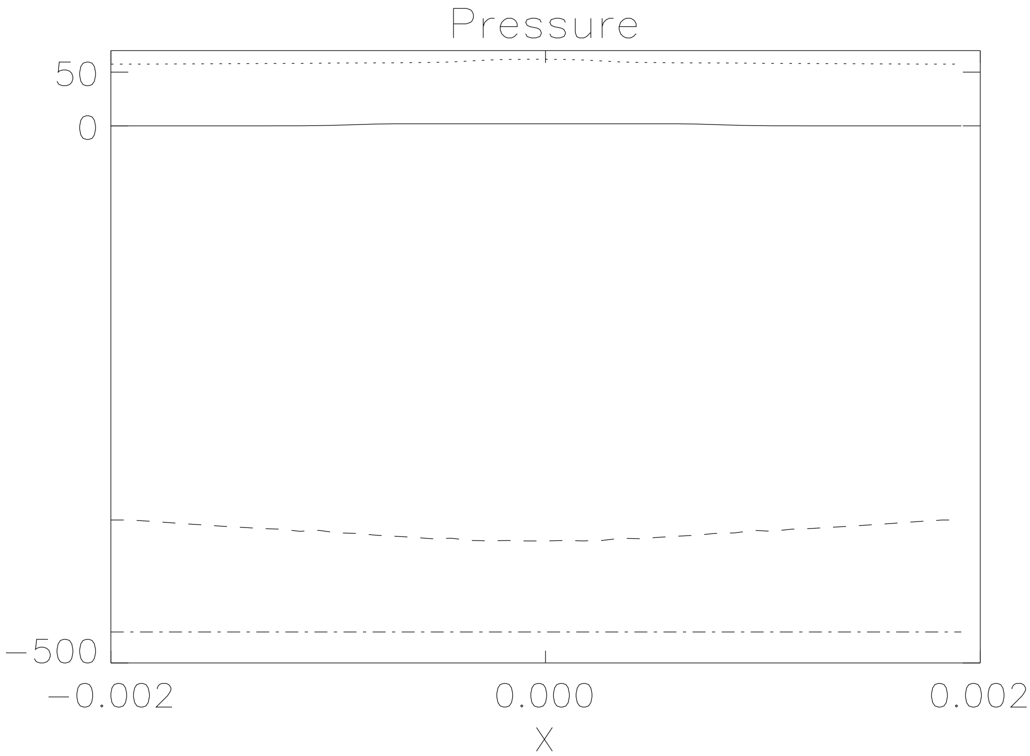

Figure 17: Sound generation by colliding flames; acoustic pressure $p - p_\infty$ at four different times, $t = 0$: solid line, $t = 8 \times 10^{-4}s$: dotted line, $t = 9 \times 10^{-4}s$: dashed line, $t = 10^{-3}s$: dashed dotted line.

preconditioning matrix to assure rapid convergence even for viscosity dominated low speed flow [40]. Low Mach number preconditioning has been applied to combustion problems [41], [42], [43]. Recently, novel techniques were reported to improve the robustness and efficiency of low Mach number preconditioners for large transient pressures [44], near stagnation points [45] and for large aspect ratio cells [46].

It is not uncommon and, in fact, advantageous to subtract the constant reference pressue p_∞ from the pressure p and to use $p - p_\infty$ in low Mach number flow in place of p [28]. On the one hand, it allows a non-singular limit of the conservative Euler and Navier-Stokes equations as the Mach number approaches zero [47], [48]. On the other hand, it allows to identify stiff terms and treat them differntly. For example, Abarbanel et al. [49] split the speed of sound squared in $p = c^2\rho/\gamma$ as $c^2 = (c^2 - c_\infty^2) + c_\infty^2$. Sesterhenn et al. [50] treat the resulting non-stiff part explicitly by an upwind method and the stiff part implicitly by a central method. Gustafsson and co-workers [51], [52], [53] use the new variable $\phi = \frac{2}{\gamma-1}\frac{c-c_\infty}{u_\infty}$ to symmetrize the isentropic Euler and Navier-Stokes equations, which reduce to the incompressible flow equations for $M_\infty \to 0$. Sesterhenn et al. [54] use the change of the conservative flow variables with respect to a constant reference state to avoid the cancellation problem caused by subtracting small differences of large quantities [28].

However, in all these approaches [49] to [54], the flow quantities are not modified and an explicit method needs many time steps to compute the steady-state for low Mach number flow. The flux splittings achieve their efficiency by treating the stiff terms implicitly and are suitable for unsteady low Mach number flow simulations provided the relative

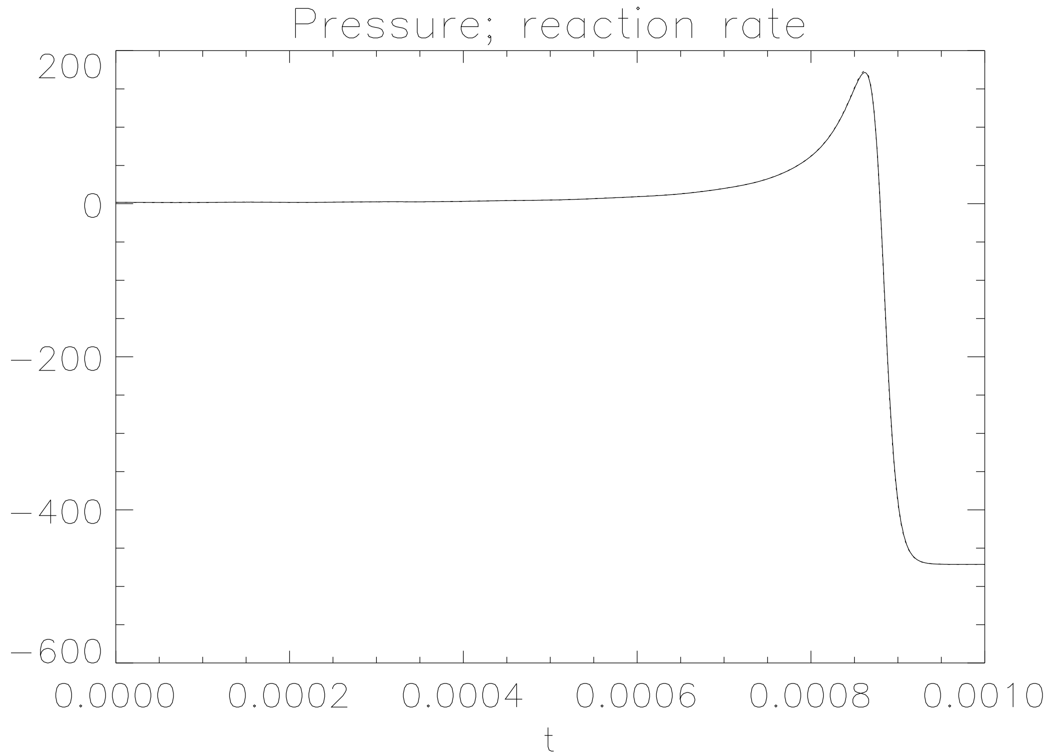

Figure 18: Sound generation by colliding flames; acoustic pressure at center $p_{center} - p_\infty$ as a function of time: solid line, linear function of heat release rate $c_1\dot{q} + c_2$ as a function of time: dashed line.

temperature changes are $\ll 1$ [49], [50] or the flow is isentropic [51], [52], [53]. Because of these restrictions, the approaches [49] to [53] are not suited for combustion. The perturbation formulation [54] removes the cancellation problem but not the efficiency problem at low Mach numbers.

We present a technique which is easy to implement, allows much larger time steps for low Mach numbers $M \ll 1$ than a non-modified explicit scheme and can also be applied for unsteady reacting flow as long as there are no acoustic effects to be simulated. For steady low speed combustion, the convergence to steady-state is considerably accelerated. This convergence acceleration by Jenny and Müller is published in [4] and [8].

The basic idea is to decrease the speed of sound artificially by subtracting a constant pressure p_0 in the entire flow field such that the modified pressure $p^\star$ is much lower than the correct pressure but still positive, i.e.

$$0 < p^\star = p - p_0 \ll p \tag{37}$$

Leaving velocity and density as well as γ unchanged, the modified speed of sound is much lower than the correct speed of sound

$$c^\star = \sqrt{\gamma \frac{p^\star}{\rho}} = \sqrt{\frac{p^\star}{p}}\, c \;\ll\; c \tag{38}$$

and the CFL condition for an explicit scheme with the Courant number σ to solve the 1D Euler equations for example becomes much less restrictive for the same spatial increment Δx

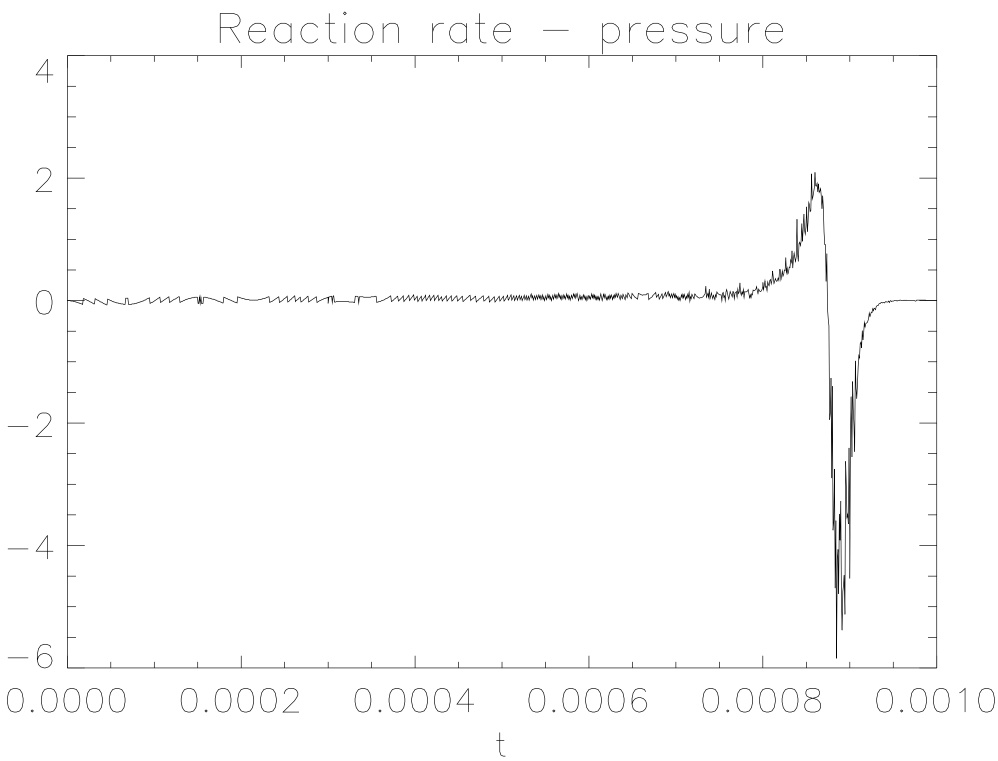

Figure 19: Sound generation by colliding flames; $p_{center} - p_\infty - (c_1\dot{q} + c_2)$ as a function of time.

$$\Delta t = \sigma\frac{\Delta x}{|u| + c} \ll \sigma\frac{\Delta x}{|u| + c^\star} = \Delta t^\star \tag{39}$$

Thus, the time step with the modified technique can be chosen much larger than with the non-modified equations. Reducing the speed of sound and keeping the velocity means increasing the Mach number

$$M = \frac{|u|}{c} \ll \frac{|u|}{c^\star} = M^\star \tag{40}$$

Therefore, we call the approach 'Mach transformation'. The constant pressure p_0 is chosen such that the modified Mach number is about

$$M^\star \approx 0.4 \tag{41}$$

to avoid to come in the transonic flow regime with possible shocks. Lowering the pressure by a constant leaves the species continuity equations and the momentum equations unchanged, if we use the correct temperature T to compute the quantities in the thermodynamic, transport and chemical models. The same conclusion applies to the energy equation, except for the inviscid part of the energy equation. The steady-state error in the energy equation can be corrected by a scalar equation, which is scaled to achieve convergence acceleration. If the scaled corrector equation is not implemented by time splitting but directly, the present convergence acceleration corresponds to a novel time derivative preconditioning which stays regular at stagnation points.

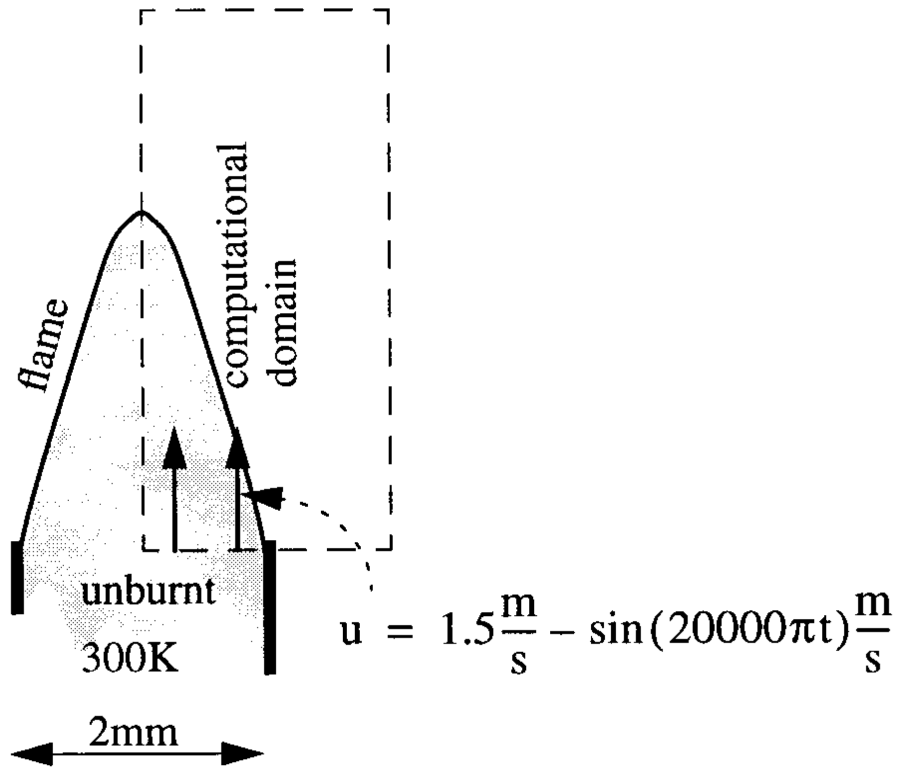

Figure 20: Unsteady 2D combustion test case; oscillating Bunsen flame.

In section 2.2, a linear stability analysis of the semi-implicit finite volume method with periodic boundary conditions is presented. The Mach number transformation is introduced in section 2.3 and interpreted as a novel inviscid low Mach number preconditioning in section 2.4. In section 2.5, convergence accelerations with the Mach transformation are demonstrated for 1D and 2D steady premixed laminar flames and an application to flame propagation is shown. Conclusions are given in section 3.2.

2.2 Stability Analysis

We analyze the stability of the semi-implicit finite volume method (15) for the scalar advection-diffusion-reaction equation with constant coefficients and periodic boundary conditions

$$\frac{\partial u}{\partial t} + a\frac{\partial u}{\partial x} - \nu\frac{\partial^2 u}{\partial x^2} = -su \ , \quad a, \nu, s \geq 0 \tag{42}$$

With the explicit first-order upwind discretization of advection, the explicit second-order central discretization of diffusion and the implicit treatment of the source term, we obtain the semi-implicit finite difference method

$$\frac{u_i^{n+1} - u_i^n}{\Delta t} + a\frac{u_i^n - u_{i-1}^n}{\Delta x} - \nu\frac{u_{i+1}^n - 2u_i^n + u_{i-1}^n}{\Delta x^2} = -su_i^{n+1} \tag{43}$$

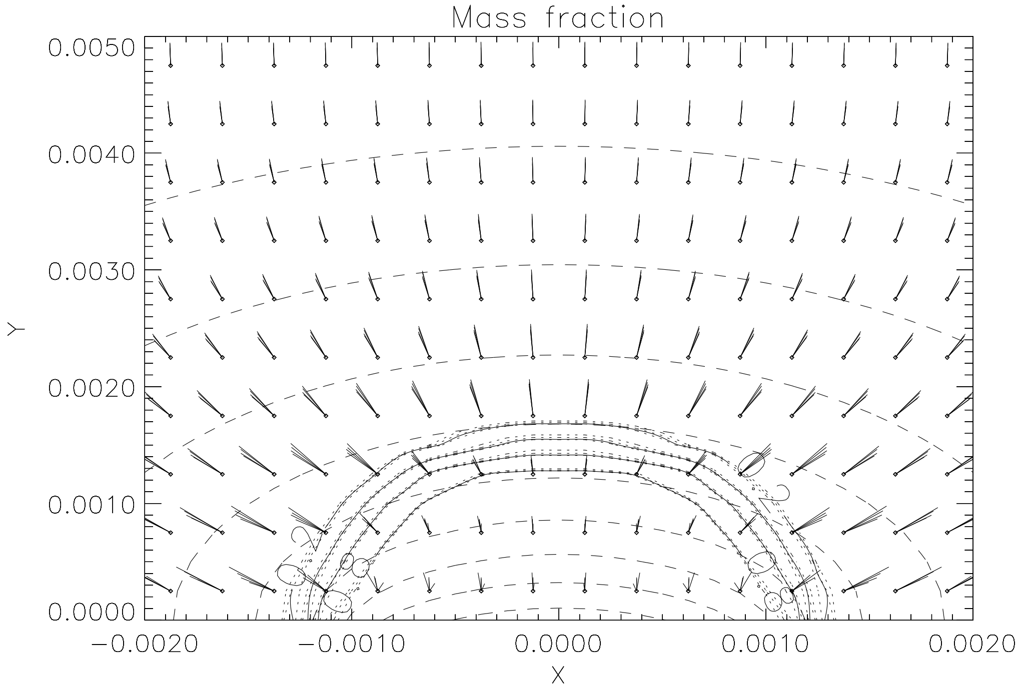

Figure 21: Oscillating Bunsen flame: mass fraction contour lines and velocity vectors at 4 different times within one oscillation. Isopotential surfaces of the acoustic field (dashed lines).

The von Neumann stability analysis yields the following stability condition

$$\sigma \left(1 + \frac{2}{Re_{\Delta x}}\right) - \frac{\mathcal{S}}{2} \ \leq \ 1 \tag{44}$$

where $\sigma = \frac{a\Delta t}{\Delta x}$ is the Courant number, $Re_{\Delta x} = \frac{a\Delta x}{\nu}$ is the cell Reynolds number and $\mathcal{S} = s\Delta t$.
The stability condition (44) shows that the semi-implicit treatment enhances stability for consumption $-s < 0$. Then, the time step can be chosen larger than for the homogeneous case $s = 0$. However, if the source term describes production $-s > 0$, the time step has to be chosen smaller than with the homogeneous case $s = 0$. For large cell Reynolds numbers $Re_{\Delta x} \gg 2$ and $-s < 0$, the stability condition (44) can be approximated by the CFL condition for the first-order explicit upwind discretization of the advection equation

$$\sigma \ \leq \ 1. \tag{45}$$

With similar arguments as in [55], the spectral radii of the coefficient matrices of the Navier-Stokes equations can be chosen as the coefficients in the model equation (42)

$$a \ = \ |u| + c, \tag{46}$$

$$\nu \ = \ max(\frac{4}{3}\frac{\mu}{\rho}, \frac{\kappa}{c_v \rho}, D_1, \cdots, D_n) \tag{47}$$

$$s \ \approx \ k_h \tag{48}$$

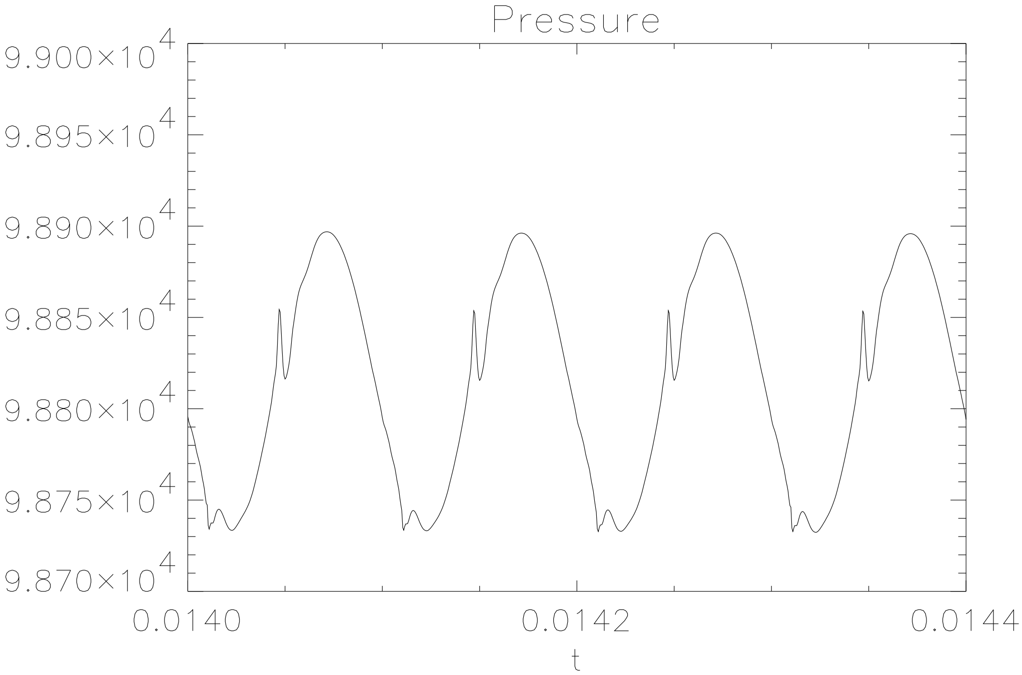

Figure 22: Oscillating Bunsen flame: pressure at tube outlet and center as a function of time.

where the reaction rate k_h is given by (17) or (6). The approximate stability condition (45) becomes

$$\Delta t \;\leq\; \frac{\Delta x}{|u| + c}. \tag{49}$$

The 2D stability analysis is given in [4]. The approximate 2D stability condition of the semi-implicit finite volume scheme (15) with first-order upwind discretization of the inviscid fluxes and second-order central discretization of the viscous fluxes reads for large cell Reynolds numbers and negative eigenvalues of the Jacobian matrix of the source term, i.e. consumption case,

$$\sigma_x + \sigma_y \;\leq\; 1, \tag{50}$$

where $\sigma_x = \frac{(|u|+c)\Delta t}{\Delta x}$ and $\sigma_y = \frac{(|v|+c)\Delta t}{\Delta y}$ are the Courant numbers in $x-$ and $y-$directions, respectively.

2.3 Mach Number Transformation

As outlined in section 2.1, we lower the speed of sound $c = \sqrt{\gamma p/\rho}$ by lowering the pressure. In the entire flow field, we lower the pressure by a constant pressure p_0 to obtain the modified pressure

$$p^\star = p - p_0. \tag{51}$$

We require $0 < p^\star$, because the modified pressure $p^\star$ is considered as an artificial thermodynamic pressure. Leaving γ and ρ unchanged, the modified speed of sound $c^\star = \sqrt{\gamma p^\star/\rho}$ becomes

$$c^\star = \sqrt{\frac{p^\star}{p}}\, c. \tag{52}$$

In order to lower the speed of sound considerably, we require $p^\star \ll p$. Thus, we choose the constant pressure p_0 such that the modified pressure $p^\star$ is as low as possible but still positive.

To determine p_0, we assume that the maximum Mach number $M_{ref} = |u_{ref}|/c_{ref}$ in the flow can be identified beforehand and that M_{ref} is a low Mach number, i.e.

$$M \ \leq \ M_{ref} \ \ll \ 1. \tag{53}$$

Then, p_0 is chosen such that the modified reference Mach number $M^\star_{ref} = |u_{ref}|/c^\star_{ref}$ is equal to a specified target Mach number $M^\star_{target}$. Using equations (52) and (51), the condition $M^\star_{target} = |u_{ref}|/c^\star_{ref}$ yields

$$p_0 \ = \ \left[1 - \left(\frac{M_{ref}}{M^\star_{target}}\right)^2\right] \ p_{ref} \tag{54}$$

If we specify $M^\star_{target} = 0.4$, the ratio of the fastest and slowest wave speeds $(0.4 + 1)/0.4 = 3.5$ is achieved for the modified reference state. Although that ratio would be slightly better (3 instead of 3.5) for $M^\star_{target} = 0.5$, we preferred the slightly safer choice $M^\star_{target} = 0.4$.

If the specific gas constant R_s and the density ρ of the mixture are not modified, the modified temperature $T^\star = p^\star/(\rho R_s)$ can be expressed as

$$T^\star \ = \ \frac{p - p_0}{\rho R_s} \ = \ T - \frac{p_0}{\rho R_s}. \tag{55}$$

Thus, we obtain the relation between the correct temperature T and the modified temperature $T^\star$

$$T \ = \ (1 + \frac{p_0}{p^\star})\, T^\star. \tag{56}$$

Only the inviscid energy equation is influenced by that modification, but neither the inviscid species continuity equations nor the inviscid momentum equations are changed. To treat the viscous fluxes $\mathbf{F}$ and $\mathbf{G}$ and the source term $\mathbf{S}$ in (10) correctly, we have to use the correct temperature T given by equation (56) to compute the temperature gradient, viscosity and thereby the diffusion coefficients and the heat conduction coefficient, the averaged specific heats, the reaction rates and the equilibrium constants. The correct temperature T is also employed to calculate γ. In short one can say that the modified pressure $p^\star$ is only used for the inviscid fluxes. For all other terms, the correct quantities are employed.

The correct total energy density $\rho E = \frac{p}{\gamma-1} + \frac{1}{2}\rho|\mathbf{u}|^2$ and the correct total enthalpy $H = \frac{\gamma p}{(\gamma-1)\rho} + \frac{1}{2}|\mathbf{u}|^2$ are related to the corresponding modified quantities (where p is replaced by $p^\star$) by

$$\rho E \ = \ \rho E^\star \ + \ \frac{p_0}{\gamma - 1} \tag{57}$$

and

$$H \;=\; H^\star \;+\; \frac{\gamma p_0}{(\gamma-1)\rho}. \tag{58}$$

Inserting equations (57) and (58) into the energy equation, we obtain

$$\frac{\partial \rho E}{\partial t} \;+\; \boldsymbol{\nabla}\cdot(\rho \mathbf{u} H) \;=\; \frac{\partial \rho E^\star}{\partial t} \;+\; \boldsymbol{\nabla}(\rho \mathbf{u} H^\star) \;+\; p_0 \frac{\partial \left(\frac{1}{\gamma-1}\right)}{\partial t} \;+\; p_0 \boldsymbol{\nabla}\cdot\left(\frac{\gamma\,\mathbf{u}}{\gamma-1}\right). \tag{59}$$

Thus, just replacing p by $p^\star$ leads to the error in the energy equation

$$p_0 \frac{\partial \left(\frac{1}{\gamma-1}\right)}{\partial t} \;+\; p_0 \boldsymbol{\nabla}\cdot\left(\frac{\gamma\,\mathbf{u}}{\gamma-1}\right). \tag{60}$$

Even if γ is constant, there is an error, because the velocity divergence is not zero for low speed combustion [28]. If we directly corrected the error (60), we would solve the correct equations but with the same low Mach number stiffness as the original equations. Thus, we would not win anything by that approach.

The new idea is to scale the modified energy equation by the ratio of the correct and modified total energy densities

$$\phi \;=\; \frac{\rho E}{\rho E^\star} \;=\; 1 + \frac{p_0}{p^\star + \frac{\gamma-1}{2}\rho|\mathbf{u}|^2}. \tag{61}$$

This equation is derived from equation (57) using the identity $\frac{1}{\gamma-1} = \frac{\rho E^\star}{p^\star + 0.5(\gamma-1)\rho|\mathbf{u}|^2}$. Using equation (54) and $M^\star_{target} = O(1)$, we can derive that

$$\phi(\mathbf{U}_{ref}) \;=\; 1 + \left(\frac{1-(M_{ref}/M^\star_{target})^2}{\beta(M_{ref}/M^\star_{target})^2}\right) \;\approx\; \frac{1}{\beta}\left(\frac{M^\star_{target}}{M_{ref}}\right)^2 \;=\; O(M_{ref}^{-2}), \tag{62}$$

where $\beta = 1 + 0.5\gamma(\gamma-1)(M^\star_{target})^2$.

Since we assume $M_{ref} \ll 1$, the parameter ϕ is very large. We get a similar result at the stagnation conditions.

The scaling factor ϕ is used to slow down the inviscid response to the heat release rate, heat conduction, enthalpy diffusion and rate of work done by the viscous forces, i.e. the right hand side of the energy equation. Therefore, the inviscid part of the modified energy equation is multiplied by ϕ. Then, after dividing by ϕ, we obtain the preliminary modified energy equation which we call 'predictor energy equation'

$$\frac{\partial \rho E^\star}{\partial t} \;+\; \boldsymbol{\nabla}\cdot(\rho \mathbf{u} H^\star) \;=\; \frac{1}{\phi}\left[\boldsymbol{\nabla}\cdot\mathbf{F}_{v\,energy} \;+\; S_{energy}\right] \tag{63}$$

Dividing the non-modified energy equation by ϕ yields

$$\frac{1}{\phi}\frac{\partial \rho E}{\partial t} \;+\; \frac{1}{\phi}\boldsymbol{\nabla}\cdot(\rho \mathbf{u} H) \;=\; \frac{1}{\phi}\left[\boldsymbol{\nabla}\cdot\mathbf{F}_{v\,energy} \;+\; S_{energy}\right] \tag{64}$$

The difference of equations (64) and (63) reads

$$\frac{1}{\phi}\,\frac{\partial \rho E}{\partial t} \;-\; \frac{\partial \rho E^\star}{\partial t} \;=\; \underbrace{(1-\frac{1}{\phi})\,\boldsymbol{\nabla}\cdot(\rho \mathbf{u} H^\star) \;-\; \frac{p_0}{\phi}\,\boldsymbol{\nabla}\cdot\left(\frac{\gamma\,\mathbf{u}}{\gamma-1}\right)}_{steady-state\ error}. \tag{65}$$

In the steady-state $\frac{\partial \rho E^\star}{\partial t} = 0$, $\frac{\partial \rho E}{\partial t}$ is not zero but equal to the steady-state error indicated in the previous equation.

However, if we add the steady-state error, i.e. the right hand side of (65) to the right hand side of (63), we get the final modified energy equation

$$\begin{aligned}\frac{\partial \rho E^\star}{\partial t} + \nabla \cdot (\rho \mathbf{u} H^\star) &= \frac{1}{\phi}[\nabla \cdot \mathbf{F}_{v\,energy} + S_{energy}] \\ &+ (1 - \frac{1}{\phi})\,\nabla \cdot (\rho \mathbf{u} H^\star) - \frac{p_0}{\phi}\,\nabla \cdot \left(\frac{\gamma\,\mathbf{u}}{\gamma - 1}\right). \end{aligned} \tag{66}$$

Thus, the modified and non-modified energy equations are related by

$$\frac{\partial \rho E^\star}{\partial t} = \frac{1}{\phi}\frac{\partial \rho E}{\partial t} \tag{67}$$

and the correct steady-state is recovered if $\frac{\partial \rho E^\star}{\partial t} = 0$. However, unless $\phi = 1$, the transient solution of the modified and non-modified energy equations differ. We can easily see that for constant γ, because if $\rho E^\star$ were the correct transient solution, equation (57) would yield $\frac{\partial \rho E^\star_{non-modified}}{\partial t} = \frac{\partial \rho E}{\partial t}$.

We can solve the modified energy equation (66) together with the correct continuity and momentum equations in one step (cf. section 2.4) or by time splitting.

Using time splitting, the correct continuity and momentum equations are solved together with the predictor energy equation (63) in the first step

$$\frac{\widetilde{\rho E}^{\star n+1} - \rho E^{\star n}}{\Delta t} = -\nabla \cdot (\rho \mathbf{u} H^\star) + \frac{1}{\phi}[\nabla \cdot \mathbf{F}_{v\,energy} + S_{energy}]. \tag{68}$$

In the second step, the scalar corrector energy equation is solved using the results of the first step $(\rho, \rho\mathbf{u}, \widetilde{\rho E}^\star)^{n+1}$ as initial conditions

$$\frac{\rho E^{\star n+1} - \widetilde{\rho E}^{\star n+1}}{\Delta t} = (1 - \frac{1}{\phi})\,\nabla \cdot (\rho \mathbf{u} H^\star) - \frac{p_0}{\phi}\,\nabla \cdot \left(\frac{\gamma\,\mathbf{u}}{\gamma - 1}\right). \tag{69}$$

For simplicity, a second-order central discretization is employed in the right hand side of equation (69).

2.4 Interpretation as Low Mach Number Preconditioning

The Mach number transformation is analyzed here for the 1D Euler equations of perfect gas. The continuity and momentum equations are unchanged. Expressed in non-conservative form they read

$$\frac{\partial \rho}{\partial t} + u\,\frac{\partial \rho}{\partial x} + \rho\,\frac{\partial u}{\partial x} = 0, \tag{70}$$

$$\frac{\partial u}{\partial t} + u\,\frac{\partial u}{\partial x} + \frac{1}{\rho}\frac{\partial p^\star}{\partial x} = 0, \tag{71}$$

where $p^\star = p - p_0$ with p_0 constant. The predictor energy equation (63) becomes in non-conservative form

$$\frac{\partial p^\star}{\partial t} + u\,\frac{\partial p^\star}{\partial x} + \gamma p^\star\,\frac{\partial u}{\partial x} = 0. \tag{72}$$

The term $\gamma p_0 \frac{\partial u}{\partial x}$ in the correct energy equation is neglected. Thus, apart from scaling the viscous and source terms by ϕ (61), the predictor energy equation (63) neglects $\gamma p_0 \boldsymbol{\nabla}\mathbf{u}$, when written in non-conservative form.

Instead of analyzing the corrector energy equation (69) for time splitting, we express the modified energy equation (66) in non-conservative form to investigate the combination of equations (63) and (69)

$$\phi\,\frac{\partial p^\star}{\partial t} + (\phi-1)(\gamma-1)\,(\frac{u^2}{2}\frac{\partial \rho}{\partial t} + \rho u\,\frac{\partial u}{\partial t}) + u\,\frac{\partial p^\star}{\partial x} + \gamma(p^\star + p_0)\,\frac{\partial u}{\partial x} = 0. \tag{73}$$

To simplify the analysis, we neglect the term $(\phi-1)(\gamma-1)\,\frac{u^2}{2}\,\frac{\partial\rho}{\partial t}$ in (73). Compared with $\phi\,\frac{\partial p^\star}{\partial t}$, the neglected term in (73) is of order $O(M^2)$ for isentropic flow. Moreover, the steady-state is not affected by adding a term proportional to $\frac{\partial \rho}{\partial t}$. Thus, instead of (73) we analyze the following simplified equation

$$\phi\,\frac{\partial p^\star}{\partial t} + (\phi-1)(\gamma-1)\,\rho u\,\frac{\partial u}{\partial t} + u\,\frac{\partial p^\star}{\partial x} + \gamma(p^\star + p_0)\,\frac{\partial u}{\partial x} = 0. \tag{74}$$

Using the definition of $p^\star$ (51), equations (70), (71) and (74) can be expressed in the form

$$\mathbf{P}^{-1}\frac{\partial \mathbf{V}}{\partial t} + \mathbf{A}\frac{\partial \mathbf{V}}{\partial x} = 0,$$

where

$$\mathbf{V} = \begin{pmatrix} \rho \\ u \\ p \end{pmatrix}, \qquad \mathbf{A} = \begin{pmatrix} u & \rho & 0 \\ 0 & u & \frac{1}{\rho} \\ 0 & \gamma p & u \end{pmatrix}, \qquad \mathbf{P}^{-1} = \begin{pmatrix} 1 & 0 & 0 \\ 0 & 1 & 0 \\ 0 & (\phi-1)(\gamma-1)\rho u & \phi \end{pmatrix}.$$

Thus, if we do not use time splitting, the Mach number transformation can be interpreted as a novel Euler preconditioner. The eigenvalues of $\mathbf{PA}$ are

$$\begin{aligned} \lambda_1 &= u, \\ \lambda_{2,3} &= (1-\gamma\frac{\phi-1}{2\phi})u \pm \sqrt{(\gamma\frac{\phi-1}{2\phi}u)^2 + \frac{c^2}{\phi} - \frac{\phi-1}{\phi}(\gamma-1)u^2}. \end{aligned} \tag{75}$$

If $\phi = 1$, i.e. no preconditioning, the eigenvalues of the correct 1D Euler equations are recovered. At a stagnation point, the eigenvalues of $\mathbf{PA}$ are 0 and $\pm c/\sqrt{\phi}$. Contrary to other time derivative preconditionings, the Mach transformation does not require any special treatment or fix at stagnation points, because the matrix $\mathbf{P}^{-1}$ is regular even at a stagnation point.

Using $\phi \approx (M^\star_{target}/M_{ref})^2/\beta$ from (62) for $M_{ref} \ll 1$, the modified acoustic wave speeds can be approximated by

$$\lambda_{2,3} = u_{ref}\left(1 - \frac{\gamma}{2} \pm \sqrt{\frac{\gamma^2}{4} + \beta(M^\star_{target})^{-2} - (\gamma-1)}\right). \tag{76}$$

For $M^\star_{target} = 0.4$, we get $\lambda_2 \approx 2.87u_{ref}$ and $\lambda_3 \approx -2.27u_{ref}$. Thus the ratio of the largest and smallest moduli of the eigenvalues of $\mathbf{PA}$ at the reference state is $\kappa(\mathbf{PA}) \approx 2.87$, opposed to $\kappa(\mathbf{A}) \approx 1 + M_{ref}^{-1}$ for the non-modified equations.

2.5 Results with Mach Transformation

We investigate the convergence acceleration to steady-state by the Mach transformation for 1D and 2D premixed laminar flames in sections 2.5.1 and 2.5.3, respectively. In section 2.5.2, we show an application of the Mach transformation to flame propagation.

To obtain the following results, the RHR flux solver of section 1. was applied. But the choice of the Riemann solver is of no importance for the following convergence studies. Any other flux discretization can be used.

2.5.1 1D Premixed Laminar Flames

To demonstrate the convergence acceleration by the Mach transformation we first use the simple 1D test case of a steady, premixed laminar flame as described in section 1.6.1. For the following simulations a uniform grid with 50 grid points was used. The temperature, velocity, mass flow and pressure profiles in Fig. 23 show that the numerical solutions, one obtained with the non-modified (dashed lines) and one with the modified scheme (solid lines), are nearly equal. The plots of the steady-state lie on top of each other.

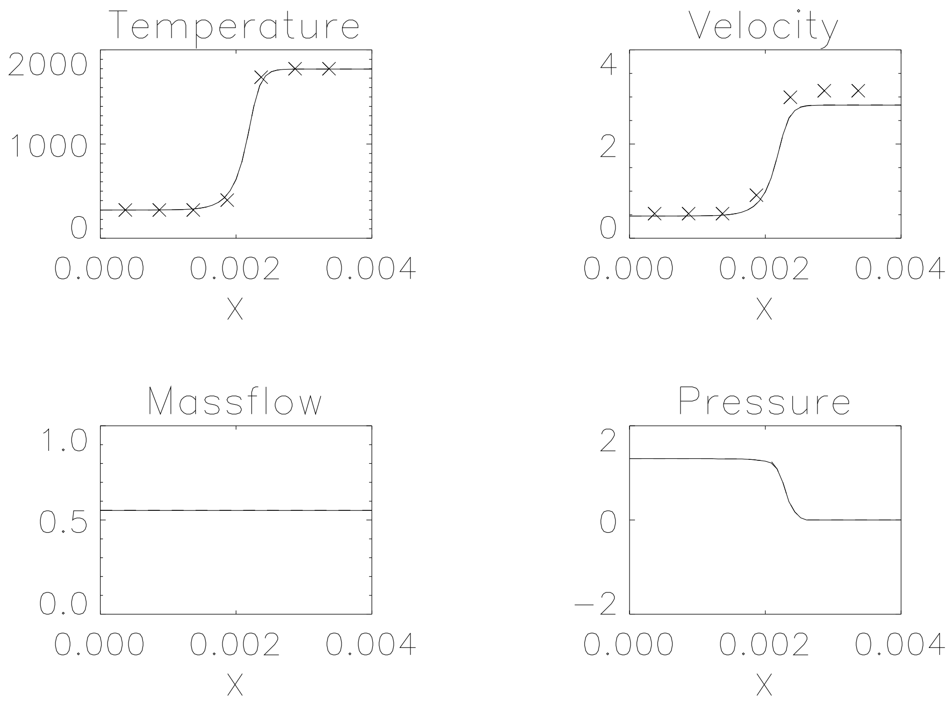

Figure 23: Steady 1D premixed laminar flame with simple chemistry; without Mach transformation: dashed line, with Mach transformation: solid line, reference solution: markers.

The modified pressure $p^\star$ was $p - 0.999 \times 10^5 Pa$ and a local Courant number of 0.8 was used. The flame Mach number $M_{flame} = M(x = 0) = 0.00136$ was correctly calculated without and with Mach transformation. The markers in the temperature and velocity plots show the results of an unsteady simulation on a uniform grid with 400 grid points [56]. The corresponding convergence histories of Fig. 24 demonstrate that more than 10 times as much CPU time was necessary to obtain steady-state (the time used to solve the additional scalar equation is negligible) with the original scheme than with the modified one. There have no studies been made how to optimize the choice of p_0 or to find a better discretization of the additional scalar equation.

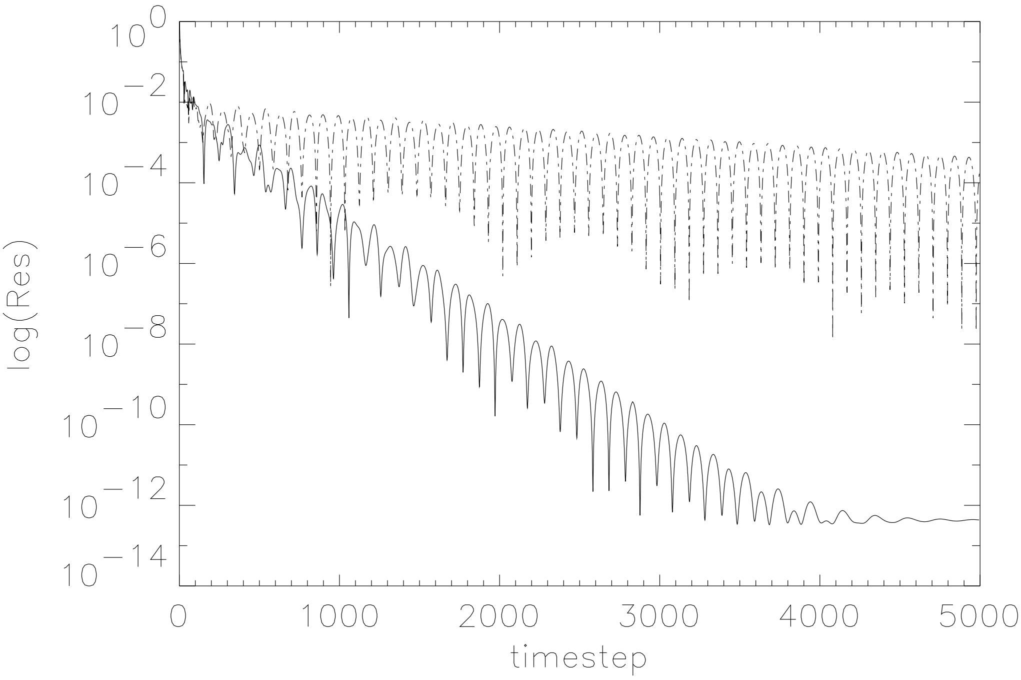

Figure 24: Convergence history of 1D premixed laminar flame with simple chemistry, 50 grid points, $CFL = 0.8$; without Mach transformation: dashed line, with Mach transformation: solid line.

To show that the method is not restricted to simulations with simple chemistry, the same studies as above were made for a hydrogen air flame described by 11 reactions and 8 species [57]. The reaction mechanism may also be found in [4] and [8].

The outlet pressure was prescribed as $p_{out} = 10^5 Pa$. The inlet boundary conditions were $Y_{H_2} = 0.0284$, $Y_{O_2} = 0.2255$, $Y_{N_2} = 0.7461$ and $T = 300K$. The inlet velocity corresponds to the flame velocity, which is a result of the steady-state flame calculation. Note that the added velocity change (18) vanishes in the steady-state, because the mass flow is constant then.

The Prandtl and Schmidt numbers are set equal to 0.7 and 0.2, respectively. The viscosity is determined with the Sutherland law. The ratio of specific heats γ is set equal to 1.4. For the standard heat of formation H_i^0 and the equilibrium constants K_h^c, the polynomials in T from the CHEMKIN library [10] are used. A uniform grid with 50 grid points was employed.

Fig. 25 shows the velocity and three radical profiles obtained with (solid lines) and without (dotted lines) Mach transformation and compares them with the results obtained with the code *premix* [58] (dashed lines) which uses the CHEMKIN library. As in Fig.

23, the numerical solutions with the two schemes are almost equal and only the solid line can be seen. The small differences between the present results and the *premix* results in Fig. 25 are mainly due to our simplified transport models.

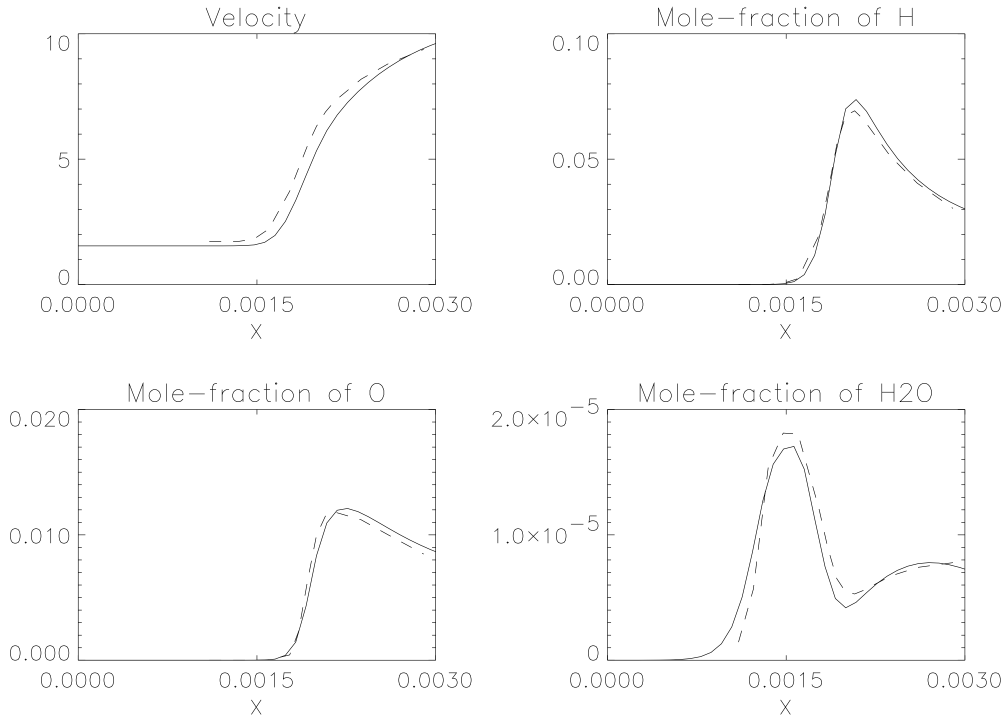

Figure 25: 1D premixed laminar flame with complex chemistry, velocity and mole-fractions; without Mach transformation: dotted line, with Mach transformation: solid line, reference solution *premix*: dashed line.

Fig. 26 shows the convergence histories of our hydrogen air flame simulations with and without Mach transformation. We see a significant convergence acceleration by the Mach transformation after about 500 time steps, when the chemistry has settled and low Mach number effects determine the convergence.

The modified pressure $p^\star$ was $p - 0.999 \times 10^5 Pa$, and a local Courant number of 0.5 was used. The flame Mach number was determined as $M_{flame} = 0.00373$ with and without Mach transformation. That value is in close agreement with the *premix* result $M_{flame} = 0.00419$

2.5.2 Flame Propagation

Fig. 27 shows a propagating laminar flame with the Mach transformation, where the temperature and velocity profiles at $t = 0s$ and $t = 0.002s$ are shown. The one-step mechanism (17) was used. Even for this unsteady flame simulation, the results with and without Mach transformation are in close agreement. The results without Mach transformation are not shown, because they are on top of the results with Mach transformation. The same p_0 as in the previous section 2.5.1 was used. The computed flame distance at $t = 0.002s$ from the initial position is close to the expected value of $u_{flame}t = 0.944 \times 10^{-3}m$. We insert $u_{flame} = 0.472m/s$ of the steady-state result with 50 grid points and not the grid

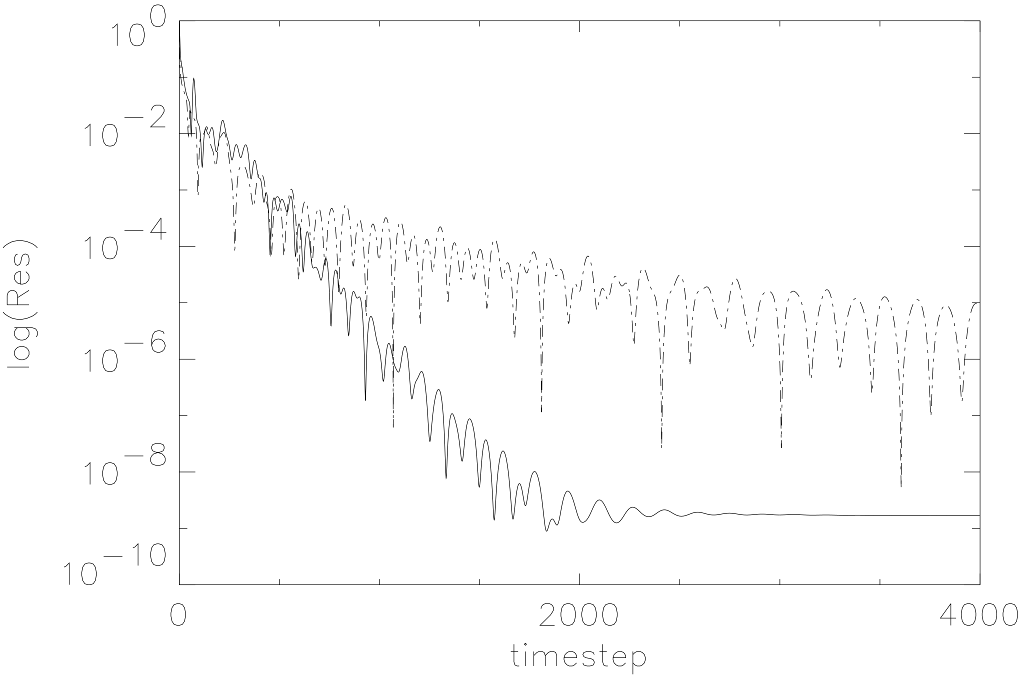

Figure 26: Convergence history of 1D premixed laminar flame with complex chemistry, 50 grid points, $CFL = 0.5$; without Mach transformation: dashed line, with Mach transformation: solid line.

converged value of $0.522 m/s$ [56], because the same 50 point grid was used for the unsteady flame simulation. The time step was $\Delta t = 2.5 \times 10^{-6} s$ for a maximum Courant number of 0.8. Therefore, 800 time steps were used with Mach transformation instead of $24,000$ time steps without Mach transformation. It is not surprising that the Mach transformation works well for this unsteady case, because no pressure waves exist there and the entropy waves are transported with the correct wave speed u according to (75). The simplified analysis leading to (75) is very well justified for this low Mach number flow.

2.5.3 2D Laminar Bunsen Flame

The last test case will show that the Mach transformation is not restricted to 1D and the same convergence acceleration is achieved in multidimensional simulations. We consider again the 2D test case of Fig. 12, which shows an infinite series of laminar Bunsen flames. The same one-step reaction mechanism (17) as in 1D and a 16×21 uniform grid was used for one symmetry half only. Fig. 28 shows the temperature contour plot with streamlines of the steady-state result, which is equal with and without Mach transformation.

However, the convergence histories of Fig. 29 indicate that about 30 times less time steps are requires with convergence acceleration. Since CPU time for the scalar corrector equation with the time splitting implementation of the Mach transformation is negligible compared with the predictor step, also the CPU time is reduced by a factor of about 30 with the Mach transformation.

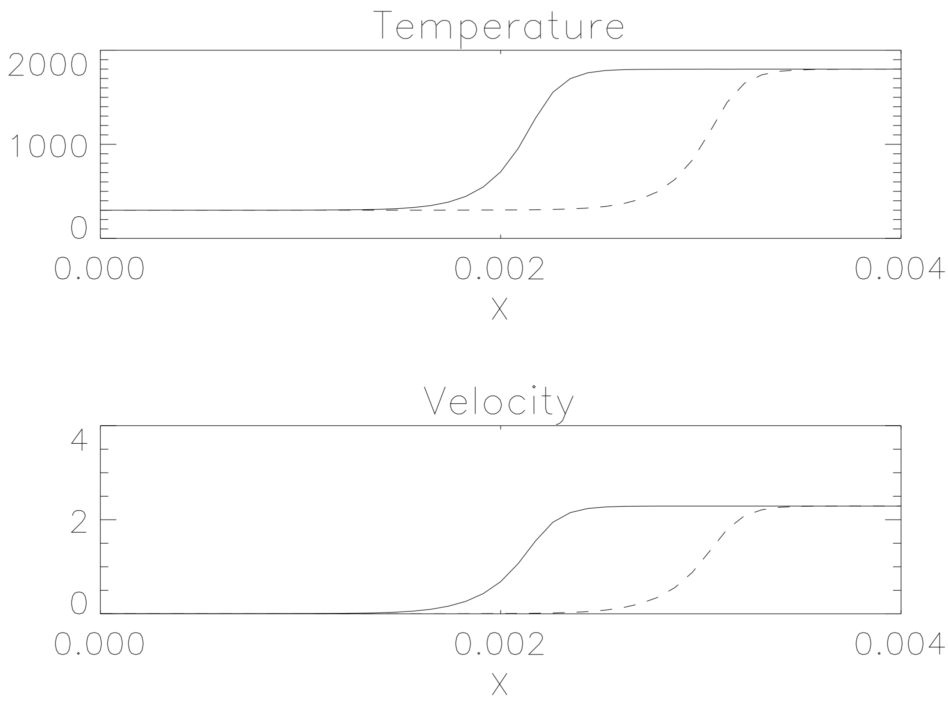

Figure 27: Flame propagation with Mach transformation; $t = 0s$: dashed line, $t = 0.002s$: solid line.

3 Conclusions

3.1 Rankine-Hugoniot-Riemann Solver

A new approach for a flux solver is presented which takes into account source terms. The source terms are distributed from the cells to the cell interfaces, where they define the flux jumps of the Rankine-Hugoniot conditions. A linearized Riemann solver yields the additional relations to determine the left and right states at the cell interfaces. For viscous and multidimensional flows, the viscous flux balance and the flux differences in the other coordinate directions, respectively, are considered as parts of the source terms. Compared with conventional Riemann solvers not taking into account source terms, the new Rankine-Hugoniot-Riemann (RHR) solver significantly improves the accuracy for a 2D Euler test case without source terms and for 1D and 2D low speed combustion simulations with stiff source terms and viscous terms. Steady-state and acoustic interactions of premixed laminar flames are calculated. The present consideration of source terms by the flux solver can be generalized to hyperbolic systems other than the Euler equations.

3.2 Convergence Acceleration

Independent of the spatial discretization, a novel technique is introduced to accelerate the convergence of compressible low Mach number flow computations to steady-state when using the Euler or Navier-Stokes equations. The stiffness due to the large disparity of the flow velocity and acoustic wave speeds is bypassed by artificially reducing the speed of sound and thereby increasing the Mach number. This Mach number transformation is

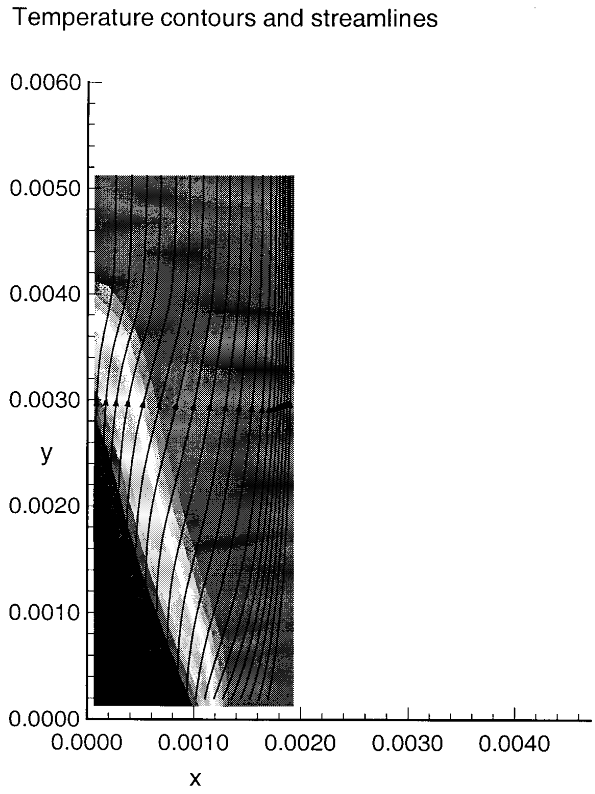

Figure 28: 2D steady laminar Bunsen flame; temperature contours with streamlines.

achieved by lowering the pressure by a constant value in the entire flow field. Only the inviscid terms in the energy equation are influenced by that pressure decrease. After scaling the modified energy equation, the steady-state error is corrected by solving a scalar equation after each time step such that the solutions of the modified and non-modified equations coincide. Thus, for each low Mach number simulation, one can obtain a convergence performance comparable to the corresponding simulation with a Mach number of about 0.4. This convergence acceleration is demonstrated for premixed laminar flames at Mach numbers of the order $O(10^{-3})$. The Mach transformation can also be applied to flame propagation, provided acoustics is of no concern. If the present technique is implemented without time splitting, it corresponds to a novel low Mach number preconditioning, which is also valid at stagnation points.

Acknowledgements

The authors thank Prof. H. Thomann, Institute of Fluid Dynamics, ETH Zürich, for the valuable discussions and encouragement throughout the course of the present research and Prof. G. Searby, IRPHE-CNRS, Marseille, for suggesting and commenting on the thermoacoustic test cases. The first author acknowledges comments on the convergence acceleration by Dr. J.G.M. Kuerten, Department of Mechanical Engineering, Eindhoven University of Technology, and by Dr. B.J. Geurts, Faculty of Mathematical Sciences, University of Twente.

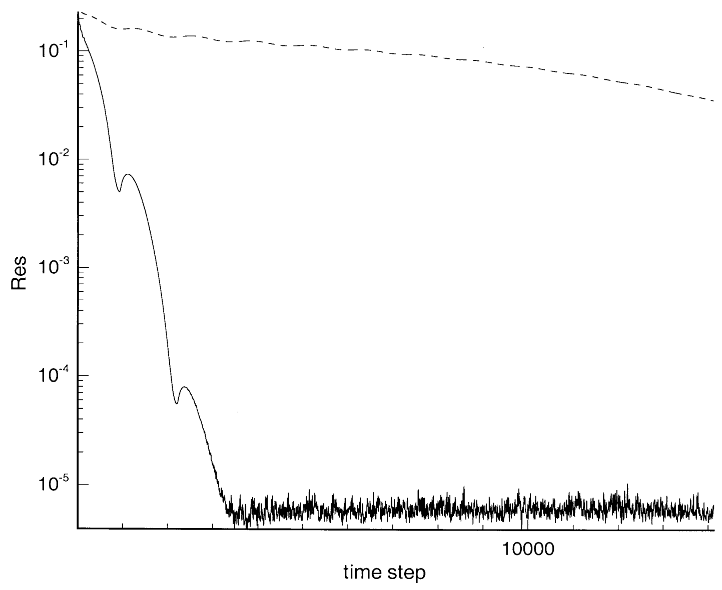

Figure 29: Convergence history of the 2D steady laminar Bunsen flame test case; without Mach transformation: dashed line, with Mach transformation: solid line.

References

[1] G. Searby. Acoustic instability in premixed flames. *Combustion Science and Technology*, 81:221–231, 1992.

[2] P. Clavin. Premixed combustion and gasdynamics. *Annual Review of Fluid Mechanics*, 26:321–352, 1994.

[3] J.J. Keller. Thermoacoustic oscillations in combustion chambers of gas turbines. *AIAA Journal*, 33:2280–2287, 1995.

[4] P. Jenny. On the numerical solution of the compressible Navier-Stokes equations for reacting and non-reacting gas mixtures. Diss ETH No. 12030 (1997).

[5] P. Jenny and B. Müller. Rankine-Hugoniot-Riemann solver considering source terms and multidimensional effects. *Journal of Computational Physics*, 145:575–610, 1998.

[6] P. Jenny and B. Müller. A new approach for a flux solver taking into account source terms, viscous and multidimensional effects. Proc. of 7th Int. Conf. on Hyperbolic Problems Theory, Numerics, Applications, Zürich, 1998.

[7] P. Jenny and B. Müller. *A New Flux Solver which Considers Source Terms and Multidimensional Effects*, pages 573–578. Proceedings of 4th ECCOMAS CFD Conference. John Wiley & Sons, Chichester, 1998.

[8] P. Jenny and B. Müller. Convergence acceleration for computing steady state compressible flow at low Mach numbers. To appear in Computers Fluids.

[9] K. K. Kuo. *Principles of Combustion.* John Wiley & Sons, New York, 1986.

[10] R.J. Kee, F.M. Rupley, and J.A. Miller. CHEMKIN-II: A Fortran chemical kinetics package for the analysis of gas-phase chemical kinetics. SANDIA Report, SAND89-8009B, 1991.

[11] E. S. Oran and J. P. Boris. *Numerical Simulation of Reactive Flow.* Elsevier, New York, 1987.

[12] R.J. LeVeque and H.C. Yee. A study of numerical methods for hyperbolic conservation laws with stiff source terms. *Journal of Computational Physics*, 86:187–210, 1990.

[13] D. Lindström. Accurate numerical solution of hyperbolic PDEs with source terms. Dissertation, Uppsala University, 1996.

[14] P. Klingenstein. Nonlinear hyperbolic conservation laws with source terms: Errors of the shock location. Diss ETH No. 12019 (1997).

[15] J. Chorin. Random choice methods with applications to reacting gas flow. *Journal of Computational Physics*, 25:253–272, 1977.

[16] P.L. Roe. *Upwind differencing schemes for hyperbolic conservation laws with source terms*, pages 41–51. Lecture Notes in Mathematics 1270. Springer-Verlag, Berlin, 1987. Eds. C. Carasso, P.A. Raviart, D. Serre.

[17] P.K. Sweby. *TVD schemes for inhomogeneous conservation laws*, pages 128–138. NNFM, Vol. 24. Vieweg, Braunschweig, 1988. Eds. J. Ballmann, R. Jeltsch.

[18] A. Bermudez and M.E. Vazquez. Upwind methods for hyperbolic conservation laws with source terms. *Computers Fluids*, 23:1049–1071, 1994.

[19] M.E. Vazquez. An efficient upwind scheme with finite volumes of the edge-type for the bidimensional shallow water equations. Proceedings of First International Symposium on Finite Volumes for Complex Applications, Eds. F. Benkhaldoun, R. Vilsmeier, Rouen, France, pp. 605-612 (1996).

[20] R.J. LeVeque. Balancing source terms and flux gradients in high-resolution Godunov methods. Submitted to Journal of Computational Physics.

[21] R.J. LeVeque and D. Bale. Wave propagation methods for conservation laws with source terms. Submitted to Proc. of 7th Int. Conf. on Hyperbolic Problems Theory, Numerics, Applications, Zürich, 1998.

[22] P. Jenny, B. Müller, and H. Thomann. Correction of conservative Euler solvers for gas mixtures. *Journal of Computational Physics*, 132:91–107, 1997.

[23] E.F. Toro. Defects of conservative methods and adaptive primitive conservative schemes for computing solutions to hyperbolic conservation laws. Technical Report MMU 9401, Manchester Metropolitan University, Department of Mathematics and Physics, 1994.

[24] P. Jenny, B. Müller, and H. Thomann. Riemann solver for compressible combustion codes. Proceedings of First International Symposium on Finite Volumes for Complex Applications, Eds. F. Benkhaldoun, R. Vilsmeier, Rouen, France, pp. 705-715 (1996).

[25] G. Fernandez, K. Z. Tang, and H. A. Dwyer. A comparative study of the low Mach number and Navier-Stokes equations with time-dependent chemical reactions. Twelfth Int. Conference on Numerical Methods in Fluid Dynamics, Springer Verlag, Berlin, pp. 490-494 (1990).

[26] J. Sesterhenn, B. Müller, and H. Thomann. *A simple characteristic flux evaluation for subsonic flow*, pages 57–61. Proceedings of 2nd ECCOMAS CFD Conference. John Wiley & Sons, Chichester, 1994. Eds. J.-A. Désidéri, C. Hirsch, P. LeTallec, M. Pandolfi, J. Périaux.

[27] J. Sesterhenn. *Zur numerischen Berechnung kompressibler Strömungen bei kleinen Mach-Zahlen.* PhD thesis, ETH Zürich Nr. 11334, 1995.

[28] B. Müller. Low Mach number asymptotics of the Navier-Stokes equations and numerical implications. 30th Computational Fluid Dynamics Lecture Series, von Karman Institute, 1999.

[29] D. Durox, F. Baillot, G. Searby, and L. Boyer. On the shape of flames under strong acoustic forcing: A mean flow controlled by an oscillating flow. *Journal of Fluid Mechanics*, 350:295–310, 1997.

[30] H. Hahnemann and L. Ehret. Über den Einfluss starker Schallwellen auf eine stationär brennende Gasflamme. *Zeitschrift für technische Physik*, 24:228–248, 1943.

[31] L.D. Landau and E.M. Lifshitz. *Fluid mechanics.* Pergamon Press, Oxford, 2nd edition, 1993.

[32] P. Jenny. An implicit 2D Navier-Stokes solver. Interner Bericht No. 5, Institut für Fluiddynamik, ETH Zürich, 1993.

[33] G. Volpe. Performance of compressible flow codes at low Mach numbers. *AIAA Journal*, 31:49–56, 1993.

[34] Ramshaw J. D. and Mousseau V. A. Damped artificial compressibility method for steady-state low-speed flow calculations. *Computers Fluids*, 20:177–186, 1991.

[35] P.J. O'Rourke and F.V. Bracco. Two scaling transformations for the numerical computation of multidimensional laminar flames. *Journal of Computational Physics*, 33:185–203, 1979.

[36] C. L. Merkle and Y.-H. Choi. Computation of low speed compressible flows with time marching procedures. *International Journal for Numerical Methods in Engineering*, 25:293–311, 1988.

[37] E. Turkel. Preconditioned methods for solving the incompressible and low speed compressible equation. *Journal of Computational Physics*, 72:277–298, 1987.

[38] B. van Leer, W.-T. Lee, and P. Roe. Characteristic time-stepping or local preconditioning of the Euler equations. AIAA Paper 91-1552-CP, 1991.

[39] E. Turkel. Review of preconditioning methods for fluid dynamics. *Applied Numerical Mathematics*, 12:257–284, 1993.

[40] D. Choi and C.L. Merkle. The application of preconditioning in viscous flows. *Journal of Computational Physics*, 105:207–223, 1993.

[41] L.-E. Eriksson. *A Preconditioned Navier-Stokes Solver for Low Mach Number Flow*, pages 199–205. 3rd ECCOMAS CFD Conference, Paris, 9-13 September 1996. John Wiley & Sons, Chichester, 1996. Edited by J.-A. Désidéri, C. Hirsch, P. LeTallec, M. Pandolfi, and J. Périaux.

[42] C.L. Merkle, S. Venkateswaran, and Y-H. Choi. Time marching computations in the complete Mach/Reynolds number domain. 13th ICNMFD, Rome, 1992.

[43] M.K. Strelets and M.L. Shur. Methods of scaling the compressibility in calculating stationary flows of a viscous gas at arbitrary Mach numbers. *U.S.S.R. Computational Mathematics and Mathematical Physics*, 28:165–173, 1988.

[44] S. Venkateswaran, P.E.O. Buelow, and C.L. Merkle. Development of linearized preconditioning methods for enhancing robustness and efficiency of Euler and Navier-Stokes computations. AIAA Paper 97-2030-CP, 1997.

[45] D. Lee, B. van Leer, and F.L. Lynn. A local Navier-Stokes preconditioner for all Mach and cell Reynolds numbers. AIAA Paper 97-2024-CP, 1997.

[46] E. Turkel. Preconditioning-squared methods for multidimensional aerodynamics. AIAA Paper 97-2025-CP, 1997.

[47] M. Hafez, M. Soliman, and S. White. A unified approach for numerical simulation of viscous compressible and incompressible flows over adiabatic and isothermal walls. "5th Symposium on Numerical and Physical Aspects of Aerodynamic Flows", Long Beach, CA, 1992.

[48] H. Bijl and P. Wesseling. *A Numerical Method for the Computation of Compressible Flow with Low Mach Number Regions*, pages 206–212. 3rd ECCOMAS CFD Conference, Paris, 9-13 Sept. 1996. John Wiley & Sons, Chichester, 1996. Edited by J.-A. Désidéri, C. Hirsch, P. LeTallec, M. Pandolfi, and J. Périaux.

[49] S. Abarbanel, P. Duth, and D. Gottlieb. Splitting methods for low Mach number Euler and Navier-Stokes equations. *Computers Fluids*, 17:1–12, 1989.

[50] J. Sesterhenn, B. Müller, and H. Thomann. Flux-vector splitting for compressible low Mach number flow. *Computers Fluids*, 22:441–451, 1993.

[51] J. Guerra and B. Gustafsson. A numerical method for incompressible and compressible flow problems with smooth solutions. *Journal of Computational Physics*, 63:377–397, 1986.

[52] B. Gustafsson. Unsymmetric hyperbolic systems and the Euler equations at low Mach numbers. *Journal of Scientific Computing*, 2:123–136, 1987.

[53] B. Gustafsson and H. Stoor. Navier-Stokes equations for almost incompressible flow. *SIAM Journal on Numerical Analysis*, 28:1523–1547, 1991.

[54] J. Sesterhenn, B. Müller, and H. Thomann. *On the Cancellation Problem in Calculating Compressible Low Mach Number Flows*, pages 408–413. 3rd ECCOMAS CFD Conference, Paris, 9-13 September 1996. John Wiley & Sons, Chichester, 1996. Edited by J.-A. Désidéri, C. Hirsch, P. LeTallec, M. Pandolfi, and J. Périaux.

[55] B. Müller. Linear stability condition for explicit Runge-Kutta methods to solve the compressible Navier-Stokes equations. *Mathematical Methods in the Applied Sciences*, 12:139–151, 1990.

[56] H. Scherer. Numerische Simulation der Ausbreitung einer laminaren Vormischflamme. Semesterarbeit, Institut für Fluiddynamik, ETH Zürich, 1992.

[57] N. Peters and J. Warnatz. *Numerical Methods in Laminar Flame Propagation.* Vieweg, Braunschweig, 1982.

[58] R.J. Kee, J.F. Grcar, M.D. Smooke, and J.A. Miller. CHEMKIN-II: A Fortran program for modeling steady laminar one-dimensional premixed flames. SANDIA Report, SAND85-8240 UC-401, 1992.